Concepts, Modeling and Control of Tidal Turbines

Mohamed Benbouzid, Jacques-André Astolfi, Seddik Bacha, Jean-Frederic Charpentier, Mohamed Machmoum, Thierry Maître, Daniel Roye

Chapter 8

Concepts, Modeling and Control of Tidal Turbines

8.1. Introduction

Of the available renewable resources, hydroelectric energy has for several years been the subject of a great deal of interest, due to the numerous advantages it offers. The strength and speed of tidal currents, which are predictable, may be known a long time in advance, which makes it far easier for this energy to be injected into electrical grids. Other direct converters of renewable resources are sensitive to meteorological conditions. On the other hand, for a tidal turbine in a given place, we will always know the first-order power which can be extracted by energy grid operators to safely provide their consumers with electricity. There is, however, a second-order effect to be taken into account – that of the ocean waves. In addition, western European countries, particularly the United Kingdom and France, offer a great many sites near the coast where this energy can be cheaply exploited [JOH 06, EU 96].

The goal of this chapter is to give a succinct presentation of the main concepts of tidal turbines, then to provide details on modeling a basic concept, and finally to introduce the details of control/command.

Chapter written by Mohamed BENBOUZID, Jacques André ASTOLFI, Seddik BACHA, Jean Frédéric CHARPENTIER, Mohamed MACHMOUM, Thierry MAITRE and Daniel ROYE.

8.2. State of the art technology in tidal turbines

8.2.1. *Basic concepts and topologies*

8.2.1.1. *Tidal turbines versus wind turbines*

The aim of a tidal turbine is to capture kinetic energy from marine or river currents, which is used to turn a submerged rotor. Thus, it is a marine transposition of a wind turbine, which captures kinetic energy from the wind. The parallel which can be established between these two technologies lies firstly in the similar designs used. Figure 8.1 (left) shows one of the largest terrestrial wind turbines in existence, the E-126 model made by German company ENERCON. Its rotor is 126 m in diameter and it has a nominal power of 7 MW and weighs 3,750 tons. Figure 8.1 (right) shows the tidal turbine developed by Norwegian company Hammerfest Strøm. Its rotor is 12 m in diameter and produces 300 kW, weighing 107 tons including the base. It has been connected to the electrical grid since 2003 in the Kalsvund Sound in the north of Norway, near to the city of Hammerfest. Both these turbines are said to be "horizontal axis", because the shaft of the blades' rotation is horizontal, parallel to the incident force. We also speak of "axial flow turbines".

Figure 8.1. *The Enercon E126 wind turbine (left) and the Hammerfest Strøm tidal turbine (right) with axial flow*

Figure 8.2 shows the wind-v-tidal turbine juxtaposition for the so-called "vertical axis" type of turbine. They are also known as "transverse flow turbines" because the incident current must be perpendicular to the axis of rotation.[1] The photo on the left shows the world's largest transverse flow wind turbine, developed by the American laboratory Sandia and installed in Gaspésie (Quebec) at Cap-Chat. It is 110 m high and produces 4 MW. The image on the right shows the prototype tidal turbine from the company New Energy Corp. (Calgary, Alberta), which is 1.52 m in diameter. It was tested in 2007. Besides the scale factor between these two turbines, there is a noticeable difference in their design: the wind turbine's blades are geometrically formed like a parabola, whereas the tidal turbine uses straight

1 The axis of rotation can therefore be horizontal.

blades. The parabolic form comes from the fact that in air, centrifugal forces are predominant over the aerodynamic forces applied to the blades. The design of the blades is calculated to cancel out flexion forces along their middle line. Thus, a skipping-rope shape is obtained, called a *troposkein*. For small wind turbines, the troposkein shape can be avoided by reinforcing the structure (Figure 8.3, left); note the helix shape, which presents a number of advantages (discussed later on). In water, the troposkein shape is not used, because hydrodynamic forces predominate (Figure 8.3, right).

Figure 8.2. *Darrieus wind turbine (left) and New Energy tidal turbine (right), with transverse flow and vertical axes*

Figure 8.3. *Turby wind turbine (left) and Harvest-Ethic tidal turbine (right) with transverse flow*

8.2.1.2. *A list of specifications for analog*

When installing a large device, such as a "farm" of wind or tidal turbines, we must take account of a number of constraints, which are usually grouped into three categories: social, environmental and economic.

The economic aspect is the keystone of any industrial project. Two major ingredients are needed for a means of production to be developed: the existence of a market and the capacity to produce electricity at a competitive cost. These factors are, however, related. For wind energy, photovoltaic energy and indeed most renewable forms of energy from which electricity can be produced, the cost of producing a kWh is still higher than with traditional forms of energy production such as gas, hydraulic or nuclear power. In this sense, and without taking environmental factors into consideration, the kWh produced is not – yet – competitive. For this reason, in most countries, development of wind energy is favored by offering an incentive rate per kWh, guaranteed over a definite length of time[2]. Tidal turbine technology has not yet matured enough to enable its cost to be precisely evaluated. Since a great many different technologies have been put forward, we must await the results of existing experiments in order to see more clearly. It is likely, however, that systems which prove to be most effective on certain sites (sea or river, isolated or not, subject to storms or not), will be less effective elsewhere.

8.2.1.3. *Respective advantages and disadvantages*

Tidal turbines essentially have three things to recommend them over wind turbines: their discretion, their compactness and the predictability of their production. Yet it must also be remembered that the global wind energy resource is not even close to the global hydroelectric resource (nearly a ratio of 1,000).

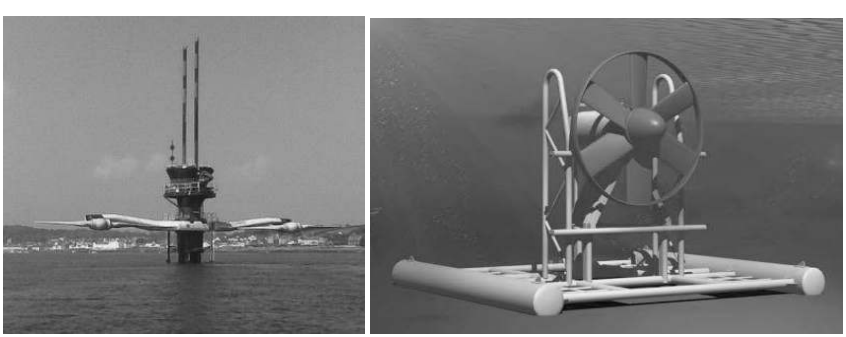

Figure 8.4. *Emerged MCT Seagen tidal turbine (left) and submerged Sabella (right)*

2 Fifteen years, in the case of France.

Although the most powerful hydroelectric facility in the world (1.2 MW, double turbine) is mounted on an emerging pile like an offshore wind turbine (Figure 8.4, left), numerous developers are now putting forward completely submerged designs (Figure 8.4, right). In this way, visual discretion is assured, at least from humans' point of view. As for the sound emission of an underwater farm, it is evaluated as being equivalent to that of a large ship.

Equation [8.1]:

$$P = \frac{1}{2}\rho C_p S V^3 \qquad [8.1]$$

shows that the power P of a turbine is proportional to the density of the environment ρ and to the cube of the velocity of the current V (C_p being the coefficient of power and S the section of the area swept by the blades of the turbine).

Considering the following conditions: 2 m/s and 1,000 kg/m^3 for water, and 10 m/s and 1.2 kg/m^3 for air, it is shown that the same power can be produced in water with a rotor smaller by a factor of 2.6 in relation to air. For example, 1 MW obtained with a rotor 50 m in diameter in air is obtained with a 19 m rotor in water with the same C_P. This leads to lighter equipment, which should be less costly. For example, the E-126 wind turbine (7 MW and 3,750 tons) produces 1.9 kW per ton, whereas the MCT Seagen tidal turbine (1.2 MW and 390 tons) produces 3 kW per ton and the Hammerfest Strøm turbine (300 kW and 107 tons) produces 2.8 kW per ton.

Besides the purely hydrodynamic reason, the compactness of a tidal turbine is also due to the fact that its operating conditions are far less subject to variability: a tidal turbine is indeed designed to exploit the quasi-maximum velocity of current (exceptional events such as floods and huge tides do not give rise to much greater velocities, but these intensities of current would not be recovered, much like extremely strong winds); in comparison, a wind turbine only exploits wind energy up to 90 km/h although its structure should withstand winds of 300 km/h.

The predictability of a tidal turbine's production is due to the fact that tidal and river currents are well known (river currents do, however, remain dependent on the weather) and have a regular nature which is not affected by the wind. River currents are constant throughout the day (excluding flood events) and tidal currents fluctuate slightly in a sinusoidal manner over a period of around 12 hours (on the European Atlantic coasts). It is therefore easier to manage the production of electricity in comparison to wind turbines, without thereby avoiding the issue of energy storage: in rivers, droughts or floods are events which impede production; for tidal energy,

slack water is a similarly unproductive period. Conversely, and in the same way as for all electricity production, the issue of storage during downtimes remains pertinent.

8.2.2. *Turbines founded on the principle of lift*

Any blade with a given profile which is immersed in a uniform current is subject to a lifting force, notated *L*, whose component is perpendicular to the incident current, and a drag force, notated *D*, whose component is along the current. The fluid potential theory shows that lift is a non-viscous phenomenon. Drag, on the other hand, brings into play a mechanism of friction between the flow threads, called dissipation. This dissipation irreversibly converts the mechanical energy of the fluid (pressure + kinetic + height energy) into thermal energy. This latter therefore represents a loss. The efficiency of a rotor, which yields mechanical energy recovered from the energy available in the fluid, will be better the less dissipation takes place. Consequently, better efficiency is generally obtained for turbines driven by forces of lift as opposed to those driven by drag.

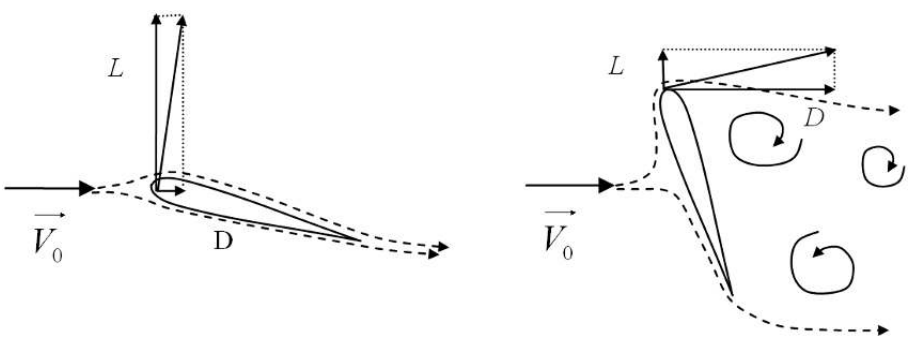

Figure 8.5. *Forces of lift (L) and drag (D) on a wing – illustration of the flows generated by lift (left) and drag (right)*

Figure 8.5 (left) represents a flow around a wind placed in a stream of low incidence. The flow threads remain close to the profile and create a de-pressurization above it (extrados) and a de-pressurization below it (intrados). This field of pressure results from the lift, far stronger than the drag. Figure 8.5 (right) represents the same profile placed in a high-incidence stream. The flow threads cannot follow the profile, they peel away. The upstream face of the profile is over-pressurized and the downstream face is under-pressurized. The drag force which results is, in that case, far greater than the lift. The vortex-shaped slipstream which develops downstream is turbulent and highly dissipative. A vertical shift in the left-

hand diagram would produce a better result than a movement to the right in the right-hand diagram.

8.2.2.1. *Axial flow turbines*

In order to better comprehend the principle on which a turbine works, the blades must be represented in cross-section in a streamtube containing the velocity vectors[3] (Figure 8.6). Thus, the blade experiences a relative upstream velocity W given by:

$$\vec{W} = \vec{V} - \vec{\omega} \wedge \vec{r} \qquad [8.2]$$

where V is the average axial velocity at the level of the rotor (lesser than that upstream) and r the radius vector joining the axis of rotation to the point considered.

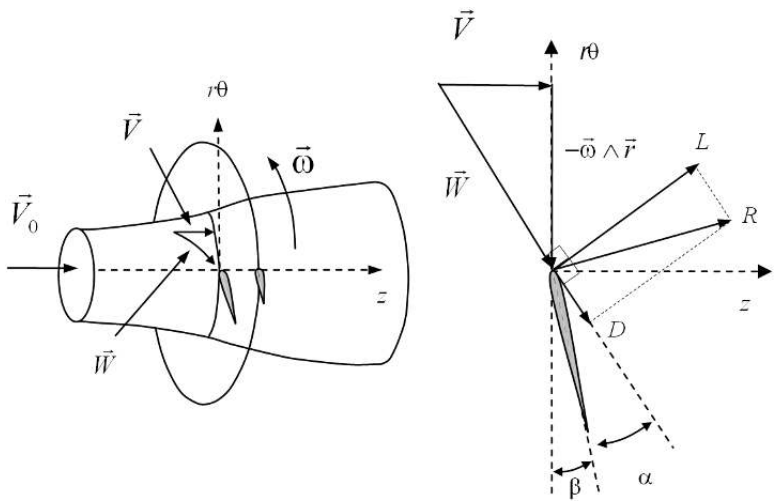

Figure 8.6. *Cross-section of the blades by a streamtube (left) and velocity triangle on the cross-section (right)*

R, which results from the forces on the section of blade, can be broken down into a lift L and a drag D. The angle β is the calibration of the section of blade and the angle α the incidence of relative flow W. Figure 8.6 shows that the torque obtained on the axis of rotation results from projecting the lift onto the axis θ diminished by projecting the drag onto the same axis. The design of the rotor consists of placing the section of blade at the best incidence so that the drag force is as small as possible in comparison to the lifting force.

3 In order to more closely reproduce the 2D situation, the components which are perpendicular to this tube are ignored.

8.2.2.2. *Transverse flow turbines*

Figure 8.7 shows a cross-section of a transverse flow turbine on a plane perpendicular to the axis of rotation. The flow is assumed to be contained within that plane.

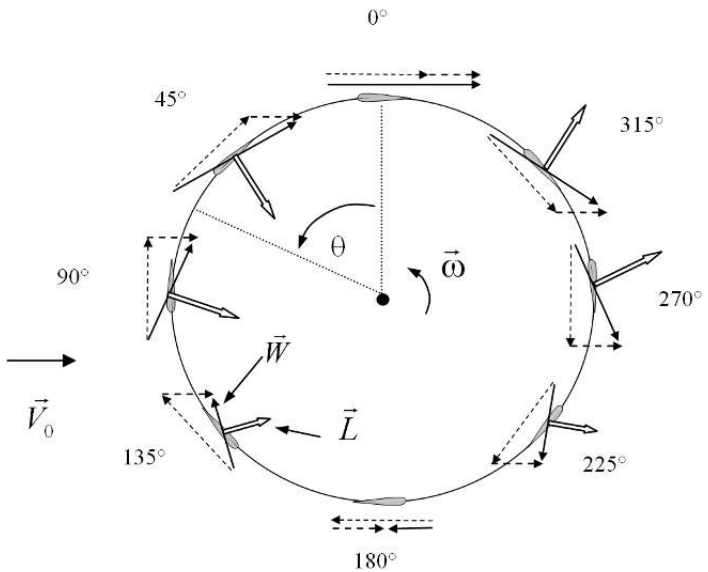

Figure 8.7. *Velocity triangles and force triangles during the rotation of a blade in a transverse flow turbine*

The horizontal dotted-line vector represents the local axial velocity at the level of the section of blade (less than V_0). The other dotted-line vector represents the opposite of the speed of rotation of the profile. The sum of these vectors, the solid-line arrow, represents the relative velocity W experienced by the profile. The difference between this and the axial flow rotor is that the profile experiences a relative flow which varies in intensity and direction during its rotation. The flow is, therefore, not stationary in the relative limits. The thickest vector represents the strain to which the blade section is subjected. Although the relative flow is not stationary and turning, the calculations are simplified by considering it to be stationary and uniform. In this context, if we also assume that there is no drag, the force experienced by the blade section is a force of line, perpendicular to W. The torque on the shaft is given by projecting this force following θ. It appears to be maximum around 90° to 135° and 270° to 315° and null around 0° and 180°; when we take the drag force into account, these two positions in reality give rise to a negative torque which applies a braking force to the turbine. The type gap between

the maximum and minimum torque will decrease as the number of blades increases. It can also be reduced by twisting the blades in a helix shape along the *z* axis. As the relative incidence of the fluid on the blade changes sign between the upstream and downstream semi-discs, so too does the radial component of the strain experienced by the blade section. Consequently, the blade is subject to a force of flexion which is directed inwards in the upstream semi-disc and outwards in the downstream semi-disc. This alternating load, which is repeated at every turn, constitutes a significant cause of fatigue.

8.2.3. *Other concepts*

8.2.3.1. *Savonius turbines and the paddle wheel*

Savonius turbines, named for their inventor in the 1920s, belong to the transverse flow group of turbines. They work with drag, as opposed to other systems which work with lift. They are generally made up of two or three cylindrical or spherical scoops, perpendicular to the wind (Figure 8.8). The motor torque comes from the drag force exerted by the flow on each of the scoops. They are often – though not necessarily – positioned vertically. The Savonius turbine is used for applications where yield is of little importance. For example, most anemometers are Savonius-type machines, because the yield plays no role at all, and the principle is used to rotate certain advertising boards. The best-known industrial application is the Flettner® ventilator, which is still manufactured widely. Placed on the roofs of vehicles, it ensures ventilation and cooling when the vehicle is in motion. At a speed of around 90 km/h, it can extract around 3 m^3 of air per minute.

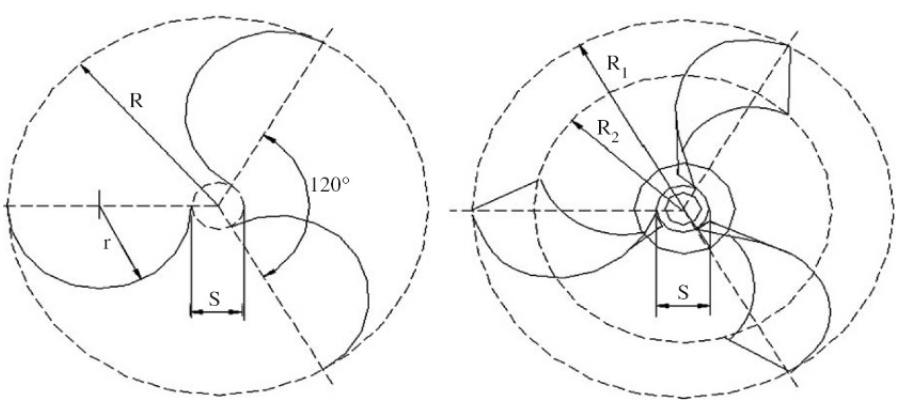

Figure 8.8. *Diagrammatic (bird's eye) view of a Savonius turbine. Left: turbine with three straight blades. Right: turbine with three twisted blades [SAH 06]*

The Savonius turbine is known for having a high startup torque, a maximum power value which is fairly feeble (in view of the area swept) but which is deemed reasonable because of its size, weight and cost for certain applications. With a performance coefficient of around 15-18% for a tip speed ratio λ near to the unit, it cannot compete with other turbines [KHA 09]. Nevertheless, its low cost, its design and its relatively simple manufacture may make it an interesting candidate for small production units of around 100 W. In [SAF 06], the authors give a good overview of various academic studies. They also show that twisting the blades improves performance, resulting in a better yield, smoother function and improved startup of the machine. To date, the Savonius turbine has no applications in the field of marine renewable energy.

8.2.3.2. *Oscillating systems*

8.2.3.2.1. VIV systems

These systems of capturing energy from tidal currents are founded on the use of the dynamic of vortexes periodically generated behind a cylinder (Figure 8.9). This phenomenon, known as VIV (for *Vortex Induced Vibration*) has been widely studied in the dynamics of fluids and structures.

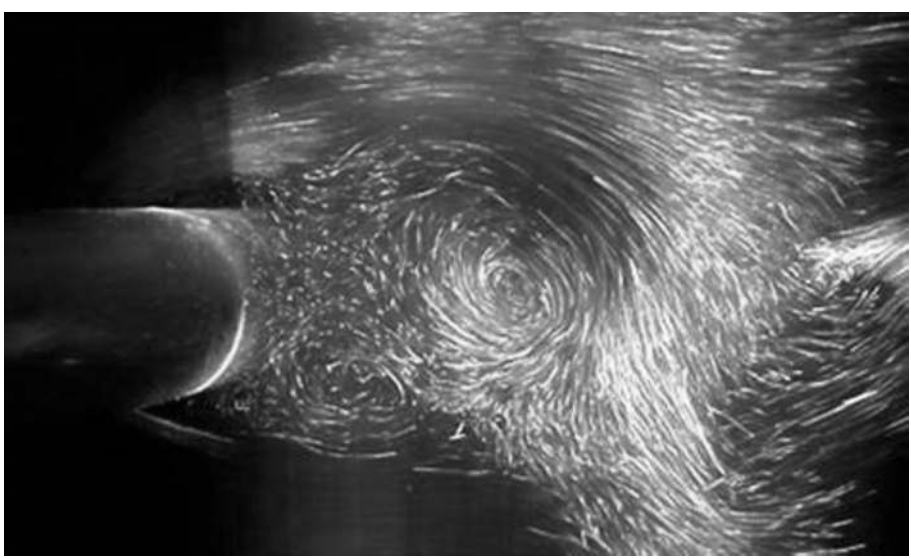

Figure 8.9. *Visual representation by fluorescent laser of the formation of a vortex behind a cylinder (Photo University of Michigan MRELab)*

This is a phenomenon which we seek to eliminate in the domain of offshore and civil engineering, for example, because of the dangers of dynamic instabilities that it can engender. It generates an oscillating lift force perpendicular to the structure, which leads to an oscillatory movement or vibration (small movement) perpendicular to the direction of the current. In certain conditions, the fluid-structure system may become unstable and lead to a significant amplification in this movement.

There exists a system which was developed and tested in a hydrodynamic basin by the University of Michigan: the VIVACE system (Vortex Induced Vibrations Aquatic Clean Energy) [BER 08]. Its designers argue, although this has still to be proven, that it is capable of extracting energy from tidal currents below two knots, where conventional turbine systems are non-operational. This low limit would allow the principle of harnessing energy from tidal currents to be extended over a far greater portion of the globe, where currents tend to be less than three knots.

8.2.3.2.2. Oscillating hydrofoil

Other oscillating systems use the force of lift generated by an oscillating wing whose incidence is controlled by an appropriate system. When tidal flow passes over it, under the effect of the lift, the wing moves perpendicularly to the flow. Up to a certain degree of incidence, the angle of incidence is actively reversed by an appropriate system; the lift is then orientated in the opposite direction, reversing the motion of the wing. This movement is reproduced cyclically. The oscillating motion of the wing drives pistons which, are linked to electrical generators via a hydraulic system.

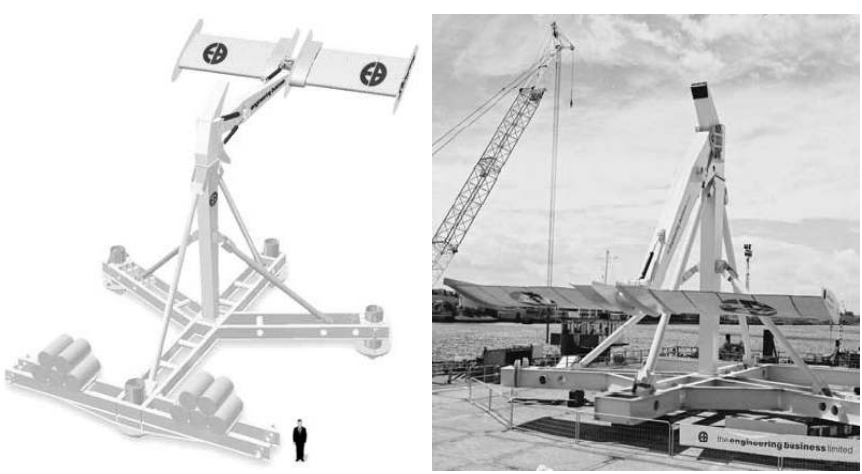

Figure 8.10. *The Stingray glider-type hydroelectric generator [BEN 09-02]*

The Stingray project (Figure 8.10), developed by Engineering Business Ltd, has seen great advances. Tests carried out in 2002 on a prototype showed an average power extracted over several cycles of around 40-50 kW for a 3.5-knot current with peaks of around 145 kW. Unfortunately, this project has been suspended since 2005.

8.2.4. *Ducts*

Ducts are fixed structures placed around the outside of a rotor to increase its power. The compactness of tidal turbines makes it easy to introduce this kind of device. Figures 8.11 and 8.12 show a number of ducted tidal turbines, using axial and transverse flow, respectively.

(a) (b) (c)

Figure 8.11. *Ducted axial flow turbines: (a) Lunar Energy (UK), (b) Alstom/Clean-Current (France), (c) Free Flow Power Corp. (USA)*

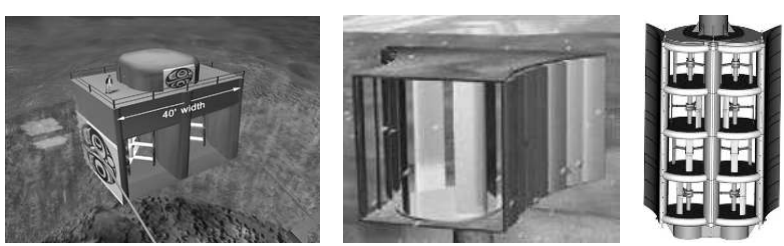

(a) (b) (c)

Figure 8.12. *Ducted transverse flow turbines: (a) Blue Energy (Canada), (b) DHVT Tidal Energy Ltd (Australia), (c) Harvest-Ethic (France)*

These ducts create a funnel effect which increased the flow rate through the rotor. The drag exerted by the fluid on the duct results in a depressurization as the flow exits it, which leads to the phenomenon of aspiration. Ducts can be classified into two types, which are distinguished by the physical origin of the drag induced by the flow:

– Venturis produce a viscous-type drag[4] due to a more-or-less pronounced detachment downstream of the duct. Mostly these are made up of straight segments which delimit portions of ducts with a constant, convergent or divergent profile. They are often symmetrical.

– Diffusers produce an inertial-type drag linked to the phenomenon of hydrodynamic lift. Diffusers are made up of profiles of wings, sometimes arranged in a cascade to increase the funnel effect; they are always asymmetrical, as either the upstream or downstream side is flared.

Figure 8.13 presents a diagram which illustrates the effect of diffuser- (left) and venturi- (right) type ducts. The dotted line represents the streamtube passing into the turbine in the absence of a duct, while the solid line is the streamtube actually exploited by the turbine with its duct. When the ducts are added, they create excess pressure outside them and a deficit of pressure inside. These effects both contribute to increasing the flowrate in the turbine. Since the power increases very rapidly with the flowrate passing into the rotor, one does not need to hugely increase the streamtube upstream in order to significantly amplify the power delivered. The coefficient of power C_p, defined in relation to the surface S swept by the turbine [8.1], may surpass the theoretical limit of 0.593 given by Betz (section 8.3.1). In the 1970s, researchers at the Grumman Aerospace Corporation (USA) using a three-bladed wind turbine equipped with diffusers in a cascade achieved a coefficient of power of 1.57, i.e. 2.65 times Betz's limit.

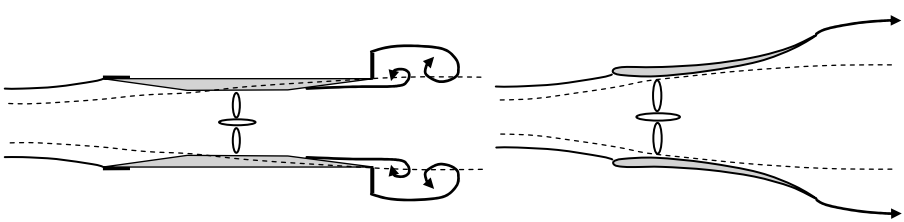

Figure 8.13. *Diffuser duct (left) and venturi duct (right)*

Let us look again at the ducted axial flow turbines in Figure 8.11. Turbines (a) and (b) are equipped with a venturi, whereas (c) has a diffuser. As for the transverse flow turbines (Figure 8.12), (a) uses a venturi whereas (b) and (c) are equipped with a diffuser. Studies on the performance of ducted tidal turbines are fewer in number than studies on wind turbines. Let us cite, in particular, the study carried out on the transverse flow DHVT (Davidson Hill Venturi Turbine) prototype, 2.4 m × 2.4 m (Figure 8.12b), which achieved a $C_{Pmax} = 0.6$, i.e. equal to Betz's limit [KIR 05].

4 This brings into play a loss of energy by viscous dissipation of the downstream vortexes.

8.2.5. *Energy potential and choice of site*

When installing a turbine, it is crucial to select the implantation site carefully. Therefore a good knowledge of the nature of marine currents is essential. There are two main types of current.

Global currents are due to differences in temperature and salinity between neighboring masses of water. They are divided into two categories: local currents, linked to winds, and regular currents such as the Gulf Stream.

So-called *tidal* currents (or tidal range currents) are found near the coasts, or in river mouths. These currents originate from the movement of the solar system's celestial bodies. They result from the gravitational interaction of the earth, moon and sun, and are directly linked to the movements of water associated with the tides. Offshore, they are gyratory, but as they approach shore they become alternative currents according to a prevailing direction. Tidal currents are generally accelerated by the topography of the seabed, particularly around capes, straits between islands and in areas with raised bottoms. It is in these latter that industrial players are particularly interested. Indeed, on these near-shore sites (less than 5 km), easy transport of the electricity is ensured by the proximity to the energy transport grids. The energy resources associated with these ocean currents are vast on a global scale. Indeed, the potential of the ocean currents which are technically exploitable is estimated to be nearly 100 GW.

This hydrokinetic energy offers the advantage of being predictable and independent of the first-order influence of meteorological variations, such as the penetration of the sun or the strength of the wind. The Scripps Institution of Oceanography (San Diego, USA), National Oceanography Centre (Southampton, UK) and the *Service Hydrographique et Océanographique de la Marine* (SHOM, Brest, France) , and other national hydrographic services elsewhere, can thus predict the fluctuations and direction of these currents for a given site years in advance, using studies of the tides and the bathymetry of the site. The surface currentological data is established depending on the geographical position using as spatial mesh. Figure 8.14 gives an example of a map of the currents in the Iroise sea for a given time and tidal coefficient.

Thus, for each spatial calculating mesh and each coefficient, it is possible to represent the current ellipse which represents the directions and amplitudes of the current speeds for each hour of the tide on a tidal cycle associated with a given coefficient (Figure 8.15). This ellipse is used to evaluate the quality of the resource in terms of the direction and amplitude of the current. If the currents' orientation does not coincide with a main axis, this can mean that certain types of turbine, such

as horizontal-axis, fixed-orientation turbines, can only extract part of the potential resource.

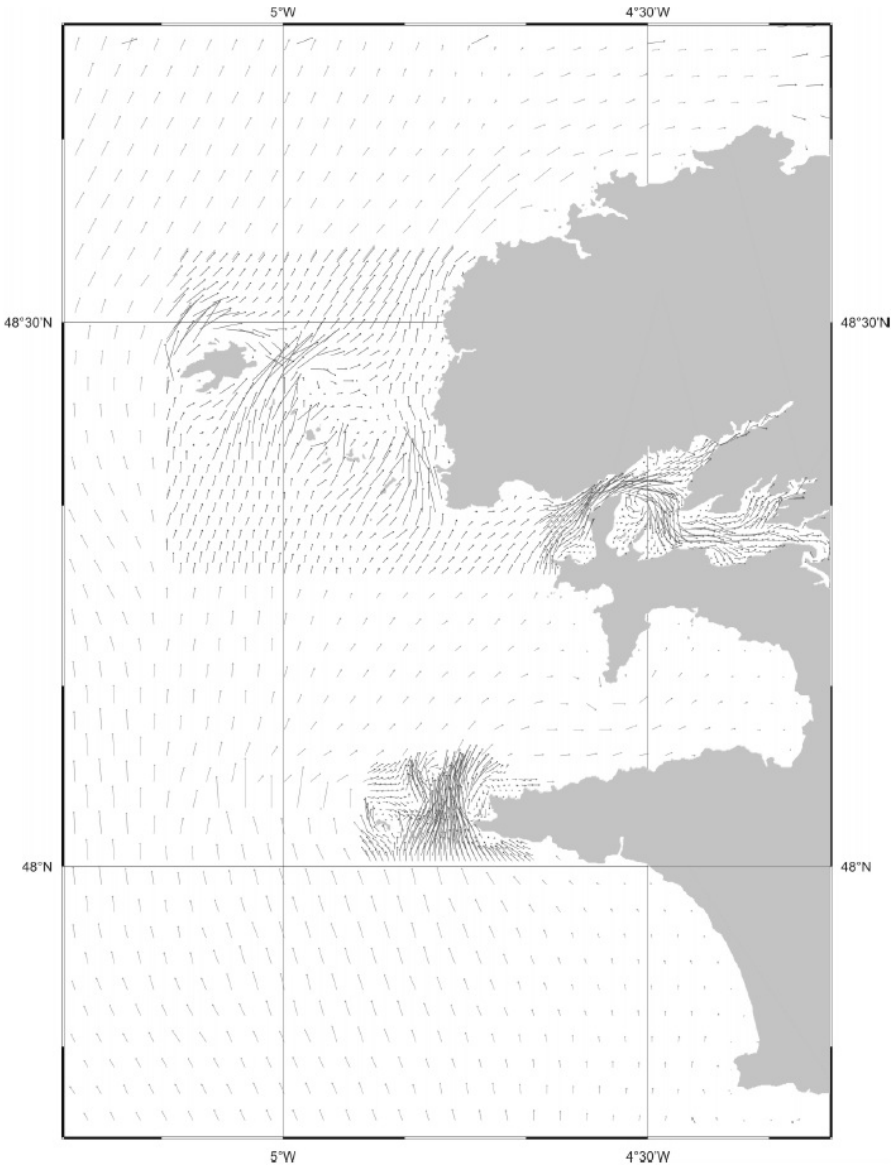

Figure 8.14. *Map showing the direction of currents for an hour of tide (Atlas de l'Iroise 560/SHOM)*

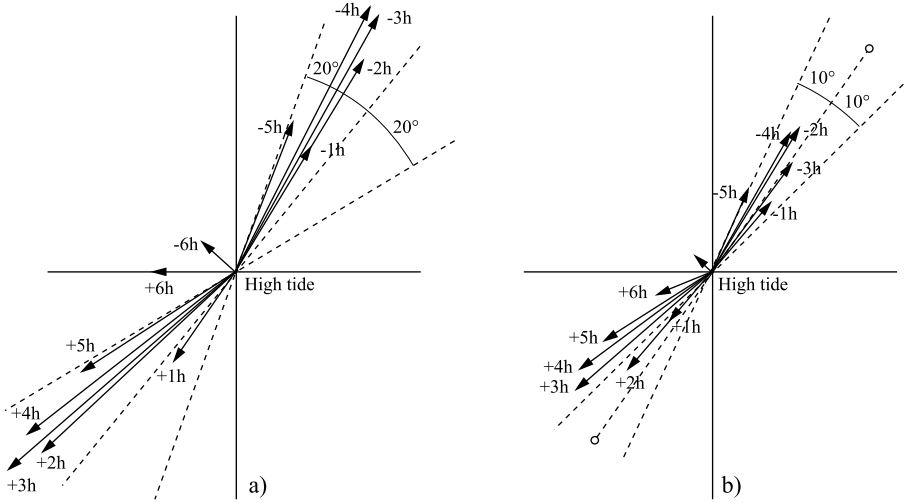

Figure 8.15. *Example of tidal ellipses for a neap tide coefficient and spring tide coefficient for a site in the Raz de Sein*

Certain areas are of particular interest, because their underwater topography gives rise to increased current speeds. The extractable power depends on the cube of the velocity [8.1], hence the advantage of choosing sites where current speeds are as high as possible. For reasons which are both technological and economic, the minimum threshold exploitable value is currently established as 1 m/second, which is about 2 knots [EU 96]. This minimum threshold may be lowered with the dawn of new technology. Nevertheless in order to avoid increased costs, the maximum current value must also be taken into account, as it corresponds to the nominal power of the system and is therefore of crucial importance in drawing up the specifications of the installation.

The choice of the site to install tidal turbines is also based on the depth of the water. The sites listed as accommodating exploitable currents are characterized by depths ranging between 30 and 40 m [EU 96]. We must also take into account variations in water level and speed due to swell, which can have a modulating effect on speeds, and more globally, to the sea state. Thus it seems that, of the different technologies hitherto proposed and studied, some are far better adapted to certain sites than to others, depending on the nature of the current ellipse, that of the seabed and the local bathymetry. The search for an optimal combination of a site and a form of technology therefore can be said to stem from an analysis of multiple criteria and multiple objectives.

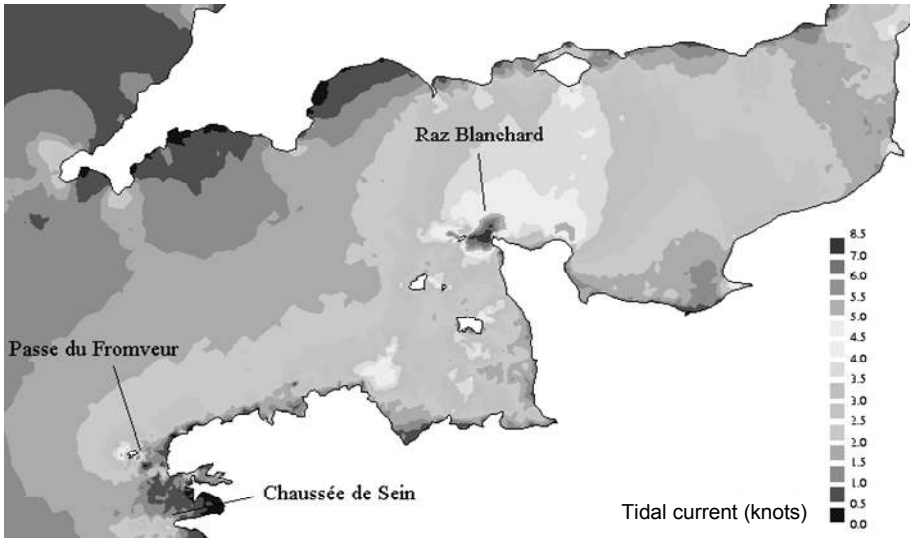

Figure 8.16. *Sites with great potential in mainland France (for a color version of this figure please see www.iste.co.uk/multon/marine.zip/)*

We have thus been able to identify three very promising sites in mainland France (Figure 8.16) [BEN 09a]: Raz Blanchard, where speeds can be up to 12 knots (6.2 m/second); the Passe du Fromveur near Ushant, with currents of around 9 knots (4.1 m/sec); and Raz de Sein, home to a north-south current which can be up to 8 knots (3.1 m/sec). It should also be noted that a great many sites along the coast of Brittany have currents between 0.5 and 3 m/second.

With a hydrokinetic resource of nearly 6 GW, distributed between Raz Blanchard (3 GW), the Passe du Fromveur (2 GW) and Raz de Sein (1 GW), France is the second-most promising country in Europe in terms of potential, after the United Kingdom (10 GW).

France's annual electricity consumption is around 450 TWh. Assuming an equivalent annual productivity with a 6 GW peak value over 2,000 hours, we get around 12 TWh. Thus, tidal turbine technology could, theoretically, cater for 2-3% of France's annual demand. Note that these figures are only theoretical (technical potential), and assume optimum exploitation of all the high-potential sites. It should also be noted that, owing to the propagation of the tide, these 3 sites if exploited together could provide relatively uninterrupted global production over a tidal cycle [BEN 08].

8.3. Modeling and control of tidal turbines

8.3.1. *Modeling*

8.3.1.1. *Elementary models of the resource*

Exploitable ocean currents are mainly created by tides and, to a lesser extent, by phenomena linked to differences in density or temperature between masses of water. The tides move huge quantities of water out to sea (ebb tide) or towards the coast (flow tides) with a period of around half a day (twice-daily cycle of 12 hours and 24 minutes) or a day (daily cycle of 24 hours and 48 minutes) depending on the site. At most sites, the phenomenon is a combination of these two major cycles. The amplitude of the tides and the currents that they generate depends on the position of the moon and sun in relation to the earth. In terms of the force of attraction, the moon's influence is around 68%, as compared to 32% for the sun. In places where the twice-daily cycle predominates, the maximum amplitudes of the currents correspond to the new moon and the full moon (during so-called "spring tides", the sun, moon and earth are practically aligned and their effects are compounded). The minimum amplitudes occur in the 1st and 3rd quarter (during so-called "neap tides", when the effects of the sun and the moon partially cancel one another out). In places where the prevailing cycle is the daily one, the amplitude of the tides depends on the declination of the moon (its height in relation to the equator). The strongest tides then correspond to large declinations and the weakest to null declinations. These variations in terms of amplitude correspond to periods of 2 weeks, a year or longer. These amplitudes are completely predictable, many months, or even many years, in advance [HAM 93].

The nature of the resource is generally derived from oceanographic databases with a geographical mesh of given resolution. For each spatial mesh, it is possible to have the main following data: velocity as a function of time for spring tides, depth, hundred year and average wave height, and distance from the coast. The first 2 values can easily reconstruct the probable speed of the current according to the date and time. Other data provide valuable information on the constraints linked to the operation of the site and the nature of possible disturbances [BRY 04].

Thus, it is possible to predict the 1st order details (without taking into account disturbances linked to the sea state), the velocity and direction of tidal currents at a point at a tidal hour using the following equation [BEN 07]:

$$\vec{V}(tt, C) = \vec{V}_{me}(tt) \frac{(C-45)(\vec{V}_{ve}(tt) - \vec{V}_{me}(tt))}{95-45} \qquad [8.3]$$

where C is the tidal coefficient, tt is the time of the tide, for the moment of calculation, $\vec{V}_{me}(tt)$ and $\vec{V}_{ve}(tt)$ are the respective velocities of the neap tides and spring tides, for coefficients of 45 and 95 at this point.

To illustrate how this kind of data can be put to use, the theoretical evolution of the amplitude of tidal currents at Raz de Sein was calculated using this method, for the year 2007 and for March 2007; the results are presented in Figure 8.17.

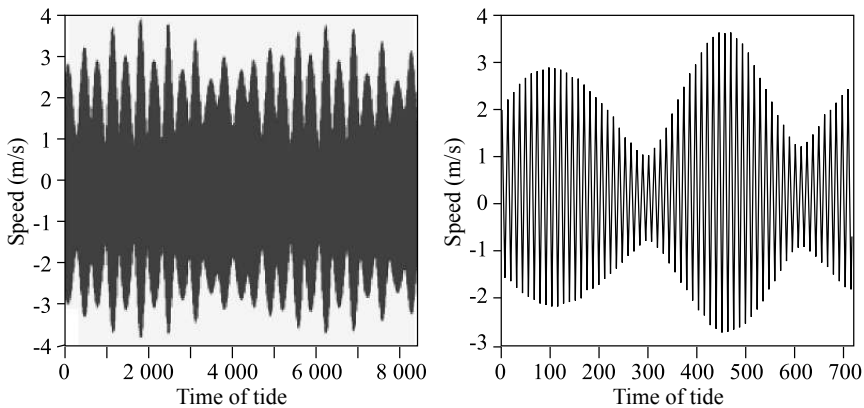

Figure 8.17. *Modeled speed of the current in the Raz de Sein over the year 2007 and for the month of March 2007*

In order to refine the technique for modeling the resource, it is possible, for example, to estimate the effect of swell. This is considered to be the disturbance which has the most profound effect on the speed of tides. For the first order, a simple Stockes model can enable us to approximate the influence of long swells on the velocity of fluid at the site. For an amplitude of monochromatic, unidirectional swell H, with period T, wavelength L and depth d (Figure 8.18) on the installation site of the tidal turbine, it is possible to calculate the value of the potential velocity Φ as a function of the depth z and from there to deduce the velocity by a spatial derivation of that potential [BEN 10a].

$$\begin{cases} V = grad\phi \\ \phi = -\dfrac{HL}{2T}\dfrac{ch2\Pi\left(\dfrac{z+d}{L}\right)}{sh2\Pi\left(\dfrac{d}{L}\right)}\sin 2\Pi\left(\dfrac{t}{T}-\dfrac{x}{L}\right) \end{cases} \qquad [8.4]$$

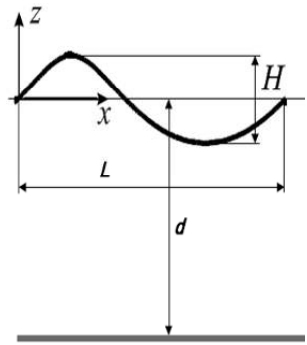

Figure 8.18. *Parameters of the Stockes model*

It should be noted that this model, which is based on the propagation of a wave with a sinusoidal surface and without disturbances in a theoretically uniform and undisturbed environment, is relatively crude and, for example, is incapable of taking into account the coupled interactions of the swell and the current.

8.3.1.2. *The 1D Approach – Betz's Theory*

The 1D theory forms the basis for the models used to design axial-flow or transverse-flow rotors. Here we present the best known example, namely Betz's theory, whereby the rotor is viewed as a disc of action creating a discontinuity in pressure. The flow in question is one-dimensional (1 streamtube) and stationary; the only energy losses from the flow are located within the rotor. Note that Betz's theory takes into account neither the shape of the system immersed in this flow nor its nature, turbine or simple grid, so long as a pressure jump can be associated with it.

Figure 8.19 presents the current lines associated with the model. For simplicity's sake, the rotor in the diagram is an axial flow turbine, but it may also be a transverse flow turbine which is *troposkien*-shaped, rectangular, etc.

V_0, V and V_1 are, respectively, the velocities upstream, in the turbine and downstream. Note that downstream, beyond the wake, the flow regains its upstream velocity V_0. The streamtube therefore houses a discontinuity of velocity in the downstream region. The pressures upstream, in front of the rotor and behind it are p_0, $p+$ and $p-$ respectively. The pressure jump from $p+$ to $p-$ is notated Δp. Note that downstream, the pressure in the wake returns to the value of the external pressure, p_0, because the current lines lose their curvature. Finally, the weight of the fluid can be integrated into the term of pressure by using the modified pressure $p^* = p + \Delta gz$.

In order to simplify its use in writing, p^* is notated p. This theory therefore applies in the case of an axis of rotation orientated in an arbitrary manner.

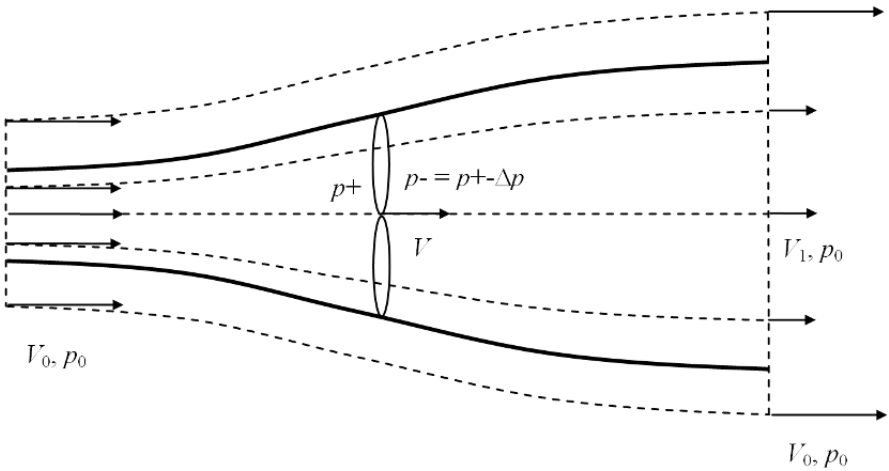

Figure 8.19. *1D diagram of flow in the case of an axial flow turbine*

Bernoulli's equation, applied upstream and down, gives:

$$\Delta p = \frac{1}{2}\rho(V_0^2 - V_1^2) \qquad [8.5]$$

The drag force F of the flow on the rotor is given by:

$$F = S\Delta p = \frac{1}{2}\rho S(V_0^2 - V_1^2) \qquad [8.6]$$

where S is the surface swept by the rotor (surface of the disc of action).

A second expression of F is obtained using the quantity of motion theorem. For an enclosed environment, this theory stipulates that the flowrate of the quantity of movement of the fluid exiting-entering is equal to the external strains applied to that environment. In the case of the environment delimited by the upstream and downstream sections and by the streamtube, we get:

$$Q(\rho V_1) - Q(\rho V_0) = -F \qquad [8.7]$$

where Q denotes the flowrate passing into the streamtube. F is the loss in the fluid's quantity of axial motion. Note that the forces of pressure around the contours of the environment, which should appear on the right-hand side of the equation, have been omitted. Their effect is shown to be null.

Using $Q = SV$, we get:

$$V = \frac{1}{2}(V_0 + V_1) \qquad [8.8]$$

The velocity in the disc of the rotor is the average of the upstream and downstream velocities. Conventionally, the induction factor a is introduced, which is an adimensional parameter representing the slowing of the fluid by the turbine.

$$\begin{cases} V = (1-a)V_0 \\ V_1 = (1-2a)V_0 \end{cases} \qquad [8.9]$$

By introducing the drag coefficient C_F, we get:

$$C_F = \frac{F}{0.5\rho S V_0^2} = 4a(1-a) \qquad [8.10]$$

With the power P being given by the product FV, we can use a similar procedure for the power coefficient C_P:

$$C_P = \frac{P}{0.5\rho S V_0^3} = 4a(1-a)^2 \qquad [8.11]$$

C_P is also known as the efficiency of the turbine. It is a measurement of the mechanical power P absorbed by the turbine, akin to the kinetic power exerted by the flow through the section S without the rotor. Figure 8.20 shows the evolution of C_F and C_P as a function of the induction factor a.

The maximum power coefficient is obtained for $a = 1/3$ and is $16/27 \approx 0.59$. A rotor, idealized by the action of the blades only and therefore not equipped with any device to increase the flow rate passing (such as ducts), can recover over 60% of the kinetic energy of the flow upstream. This is Betz's limit. The corresponding drag

coefficient is 8/9 ≈ 0.89. For a = 0.5, the drag coefficient reaches the maximum value of 1. Beyond a = 0.5, the drag decreases. In reality, the solution makes no sense in physical terms because the velocity V_1 in the wake is negative. In practice, this theory is invalid when a is greater than 0.4.

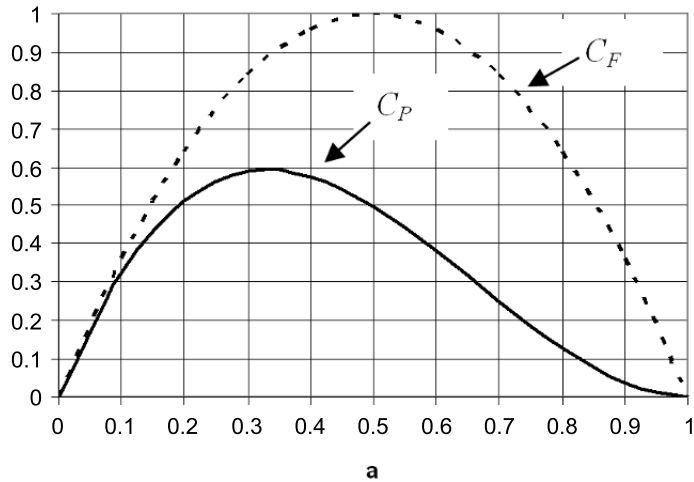

Figure 8.20. *Power and drag coefficients as a function of a*

8.3.1.3. *Modeling a horizontal-axis hydrodynamic collector*

8.3.1.3.1. Making an equation

In his original theory, Glauert uses the factors of axial and azimutal induction, notated a and a' respectively, as unknowns [GLA 35]. In the following equation, Glauert's theory is described using the variables h and k given by [LEG 08]:

$$\begin{cases} k = 1 - 2a \\ h = 1 + 2a' \end{cases} \qquad [8.12]$$

The flow at the level of a blade, in the streamtube dr, is presented in Figure 8.21. β designates the angle of calibration of the profile with direction θ, α the angle of relative velocity with the chord line of the profile (incidence) and ϕ the angle of relative velocity with direction θ. We then get the following relationships:

$$\begin{cases} \phi = \alpha + \beta \\ tg\phi = \dfrac{(1+k)}{\lambda(1+h)} \end{cases} \qquad [8.13]$$

The load *dR*, experienced by the blade section, is broken down into lift *dL* and drag *dD* given by:

$$\begin{cases} dL = \frac{1}{2}\rho W^2 c C_L dr \\ d\mathrm{D} = \frac{1}{2}\rho W^2 c C_D dr \end{cases} \qquad [8.14]$$

where C_L and C_D denote the statistical lift and drag coefficients of the blade profile and *c* its chord line with radius *r*. The number of blades is notated *N*. The drag force *dF* and the torque *dC* of the *dr* element of rotor are given:

$$\begin{cases} dF = \frac{N\rho W^2 c C_L dr \cos(\phi - \varepsilon)}{2\cos\varepsilon} \\ dC = \frac{Nr\rho W^2 c C_L dr \sin(\phi - \varepsilon)}{2\cos\varepsilon} \end{cases} \qquad [8.15]$$

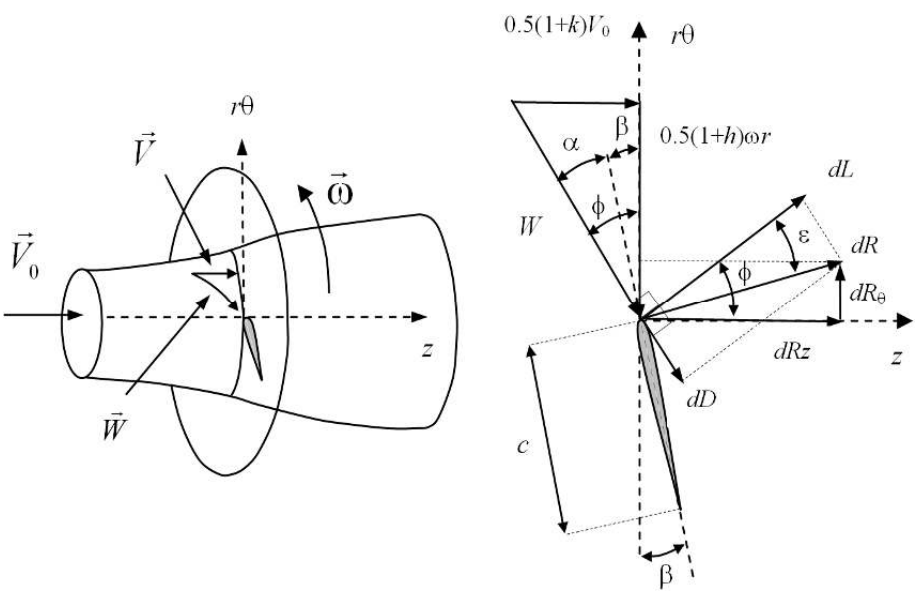

Figure 8.21. *Flow at the level of a blade in the streamtube dr*

By applying the quantity of motion theorem to the streamtube *dr*, we can determine a second expression for the drag force *dF* and the torque *dC*:

$$\begin{cases} dF = 2\pi\rho r dr V(V_0 - V_1) = \dfrac{4\pi\rho r dr W^2 \sin\phi^2 (1-k)}{(1+k)} \\ dC = 2\pi\rho r^3 dr V \omega (h-1) = \dfrac{4\pi\rho r^2 dr W^2 \sin\phi\cos\phi (h-1)}{(h+1)} \end{cases} \quad [8.16]$$

We then have two expressions for the drag and the torque of the *dr* element of rotor: the first resulting from the hydrodynamic coefficients of the generic blade section and the second from the quantity of motion theorem. By identifying the drag and the torque obtained by each method, we get:

$$\begin{cases} \sigma C_L = \dfrac{4\cos\phi\tan\phi^2}{1+\tan\phi\tan\varepsilon}\dfrac{(1-k)}{(1+k)} & \text{(Identification of the drag)} \\ \sigma C_L = \dfrac{4\cos\phi\tan\phi}{\tan\phi-\tan\varepsilon}\dfrac{(h-1)}{(h+1)} & \text{(Identification of the coupling)} \end{cases} \quad [8.17]$$

with σ the solidity at the radius *r* defined by: $\sigma = \dfrac{Nc}{2\pi r}$

The relationships in [8.17] form the basis for the calculations of the dimensions of the rotor. This is done in two stages:

– Stage of geometric definition of the optimal rotor: we calculate the element of power *dP* provided by the section *dr* of the rotor:

$$dP = \underbrace{\pi\rho r dr V_0^3}_{dP_{ref}} \underbrace{\lambda^2 (1+k)(h-1)}_{C_P} \quad [8.18]$$

dP is the product of a reference power, which depends only on the upstream velocity, and a power coefficient local to the radius *r*, C_p. We consider the ideal rotor, for which the blades do not develop drag ($\varepsilon = 0$). *h* and *k* are therefore linked and the coefficient C_p is written:

$$C_p = \lambda^2 (1+k)\left[\sqrt{1+\frac{1+k^2}{\lambda^2}} - 1\right] \quad [8.19]$$

By deriving C_p in relation to k, for each value of λ, we obtain the optimum values of k and h for the ideal rotor. For the angle of calibration β of the blade sections, we proceed thus: the angle ϕ is given by [8.13]. The angle of incidence corresponds to that which gives the best relationship C_L/C_D, i.e. the thinnest blades. This angle depends only on the hydrodynamic characteristics of the generic blade profile. The angle of calibration β is then given by relationship [8.13].

– Stage of calculation of the performances of the real-world turbine ($\varepsilon \neq 0$): the coefficients of drag C_F, moment C_M and power C_P as well as the coefficient C_B, which gives the portion of the blade surface on the disc, are given by:

$$\begin{cases} C_F = \dfrac{2F}{\rho S V_0^2} = \dfrac{2}{\lambda_0^2} \displaystyle\int_{\lambda_{0\min}}^{\lambda_0} \left(1-k^2\right)\lambda d\lambda \\ C_M = \dfrac{2C}{\rho S R V_0^2} = \dfrac{2}{\lambda_0^3} \displaystyle\int_{\lambda_{0\min}}^{\lambda_0} (1+k)(h-1)\lambda^3 d\lambda \\ C_P = \dfrac{2P}{\rho S V_0^3} = \dfrac{2}{\lambda_0^2} \displaystyle\int_{\lambda_{0\min}}^{\lambda_0} (1+k)(h-1)\lambda^3 d\lambda \\ C_B = \dfrac{B}{\pi R^2} = \dfrac{2}{\lambda_0^2} \displaystyle\int_{\lambda_{0\min}}^{\lambda_0} \sigma\lambda d\lambda \end{cases} \qquad [8.20]$$

where B is the surface of the blades, with $\lambda_{0min} = \omega r_{min}/V_0$ and $\lambda_0 = \omega R/V_0$ the tip speed ratio at the minimum r_{min} and maximum R radiuses of the rotor (λ_{0min} takes into account the influence of the hub). Note that we consider any tip speed ratio λ_0, to obtain performances outside the optimum as well. Since the geometry of the blades is fixed, the incidence α is given by [8.13]. C_L is then known and h and k are determined iteratively using [8.17].

Figure 8.22 shows the results obtained for the ideal rotor. The quantity $27C_P/16$ is presented in order to normalize C_P in relation to Betz's limit, equal to 16/27. The influence of the hub has been overlooked ($\lambda_{0\min} = 0$). We see that axial flow turbines functioning at a low tip speed ratio λ_0 experience a slight loss of power. This results from the fact that the torque of the turbine is strong, inducing a great degree of rotation in the wake. In this case, it may be interesting to join a second counter-rotative rotor to the first rotor in order to recover the kinetic moment downstream. The blade surface diminishes rapidly when the tip speed ratio increases. For the ideal rotor, the design then consists of increasing λ_0 in order to increase the hydrodynamic efficiency and therefore the power, while at the same time decreasing the blade surface. The limitation results from the mechanical performance of the

blades. Indeed, since the drag C_F hardly varies at all with λ_0, increasing λ_0 leads to the same strain being applied to thinner blades.

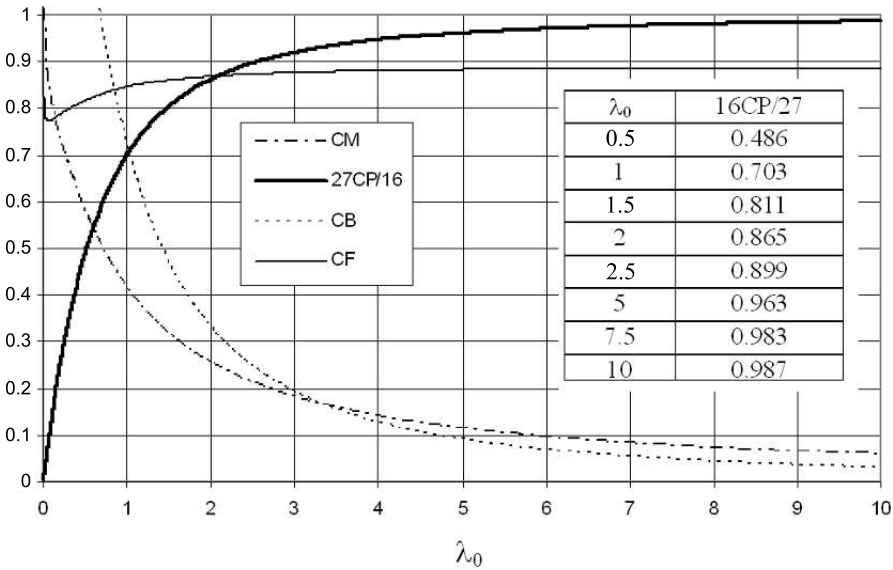

Figure 8.22. *$27C_P/16$, C_M, C_F and C_B*

Figure 8.23 presents the coefficients of power of real rotors whose generic profile blade is the NACA0018. The influence of the rotor at the radius is 10% of the maximum radius. The rotors in question have optimal tip speed ratios ranging from 4 to 10 in steps of 1. The solid curves correspond to the maximum thinness of 65 presented by the profile NACA0018 at Reynold's = 10^6. The curves in thin lines and dotted lines respectively correspond to a thinness of 120 and 500.[5] Note that 120 is an upper limit obtained on so-called laminar profiles whose surface is perfectly polished.

For the thinness of 500, the C_P is practically identical to that of the ideal rotor; note, however, that this distance increases at high tip speed ratios because of friction. The thinner the blades, the greater the distance from the ideal C_P. At a thinness of 120, the maximum C_P is fairly stable. In this case, the loss due to friction is compensated by the reduction in the rotation in the stream current after passing through the turbine. In practice, thinness tends to be around 65. In this case, the increase in λ_0 leads to a loss of power. As for the ideal rotor, we seek to make the

5 For these levels of thinness, the CD curves of the NACA0018 are simulated.

blades lighter and increase λ_0. The limitation results from the resistance of the blades but also from the loss of power induced. For tidal turbines, the limitation of λ_0 due to the resistance of the blades will be greater than for wind turbines because the loads are greater in water than in air. The rotor will therefore turn at lower tip speed ratios and its solidity (number of blades) will be greater.

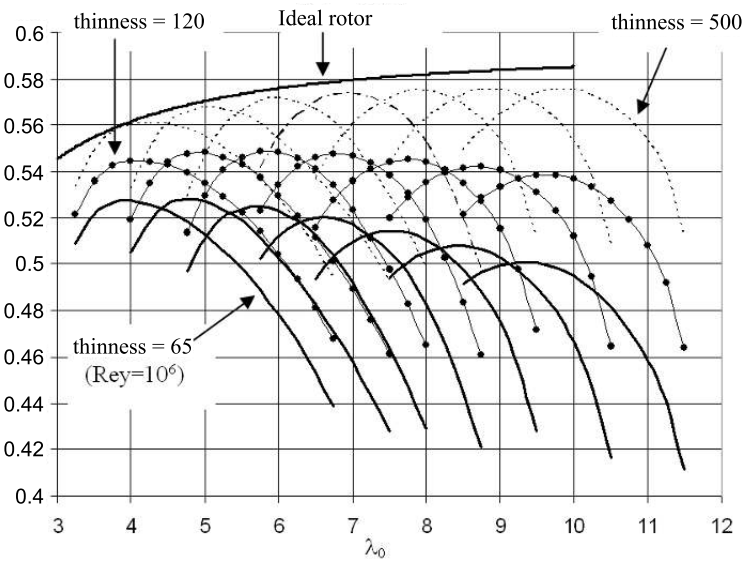

Figure 8.23. *C_P of rotors with various optimal tip speed ratios*

8.3.1.3.2. Determining the optimal incidence

The efficiency of the rotor is maximum when relationship C_L/C_D, i.e. the thinness of the blade section, is maximized. Figure 8.24 shows the C_L, the C_D and the thinness divided by 100 for the symmetrical profile NACA0018 used in the previous calculations. Three Reynold's numbers are looked at: 3.6 10^5, 10^6 and 2 10^6.

Note the slight improvement in thinness as the Reynold's number grows. The maximum thinness values are obtained for $\alpha_{opt} = 8°$ and are respectively 50, 65 and 76 for *Rey* = 3.6 10^5, 10^6 and 2 10^6. If this profile is used for the rotor, in the interests of optimal performance, the sections must have an incidence α_{opt}. In fact, this choice leads to over-sized chord lines at the hub. In practice, α must be increased at the point of the blade, this increases lift and, consequently, reduces the chord line. The laws used have only a very slight effect on the power coefficient of the rotor.

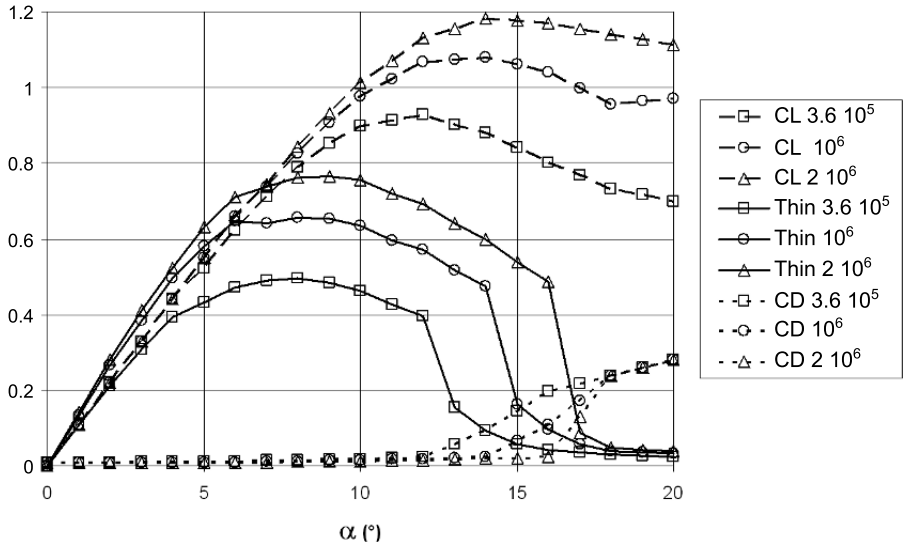

Figure 8.24. *Hydrodynamic coefficients of the NACA0018, at Rey = 3.6 10^5, 10^6 and 2 10^6*

In general, slightly arched profiles are used because they present a better degree of thinness than symmetrical profiles. For example, one might cite the profile NANA63-415 whose thinness is 120 at 4° for a Reynold's number of 3 10^6 [ABB 59]. The thinness is highly sensitive to the surface state of the profile. When the profile is perfectly polished, part of the boundary layer remains laminar with low incidence (we speak of a laminar profile) which facilitates an excellent thinness of 120. For standard roughness, the boundary layer becomes turbulent and the thinness drops to 67. This is again similar to the thinness value of the profile NACA0018 (for Rey = 10^6) discussed above, which is not a laminar profile.

8.3.1.4. *Modeling a transverse-flow hydrodynamic collector*

Flow in transverse-flow turbines is more complex than in axial-flow turbines. Figure 8.25 (left) shows a diagram of the vortex structures observed during experiments on an axial-flow rotor. The blades eject counter-rotative vortex structures the largest of which (a-b in the figure) has almost the same radius as the turbine itself. These vortexes result from dynamic detachment to which the blades are subject when rotating. The right-hand figure shows the typical variation of the power coefficient depending on the tip speed ratio. Three regions are identified: the region of deep dynamic detachment at low speed, the region of secondary effects and high speed and a transition region around the optimum speed.

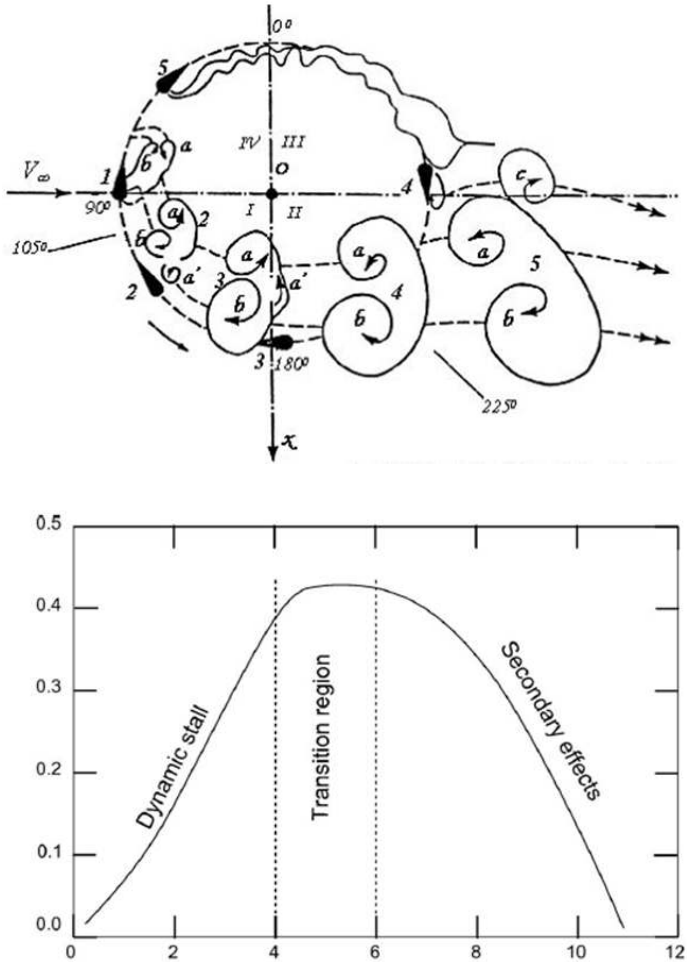

Figure 8.25. *Vortex-type structures (right) [BRO 86], regions of function (left) [PAR 02]*

These regions are linked to the angle of incidence experienced by the blade profile when rotation. For a profile whose chord line is a tangent to the disc of rotation (Figure 8.26), the geometric incidence is given by:

$$\begin{cases} \alpha = \tan^{-1}\left(\dfrac{\sin\theta}{\cos\theta + \lambda_0}\right) \\ \lambda_0 = \dfrac{\omega r}{V_0} \end{cases} \qquad [8.21]$$

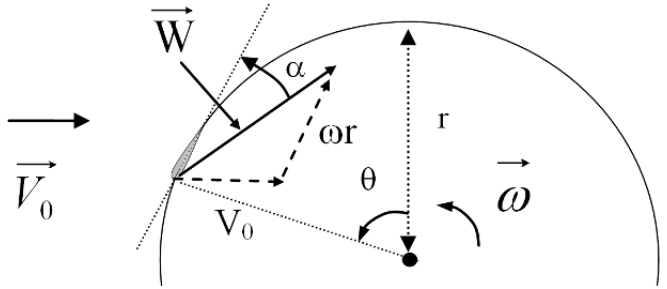

Figure 8.26. *Angle of geometric incidence experienced by the profile*

Figure 8.27 gives α as a function of θ for different tip speed ratios λ_0. The maximum incidence is between $\theta = 100$ and 140°. It increases rapidly when the specific speed decreases. In particular, the angle of static detachment typical of a profile, $\alpha = 12°$, is attained for $\lambda_0 = 5$. For a tip speed ratio less than 5, the fluid threads detach from the blade. This region is dominated by the dynamic detachment. Conversely, for a value greater than 5, the fluid threads follow the contour of the blade. This is the region of secondary effects dominated by the friction of the fluid on the blades (and the rotating parts). The maximum power is obtained in a transition region where the two effects mutually compensate.

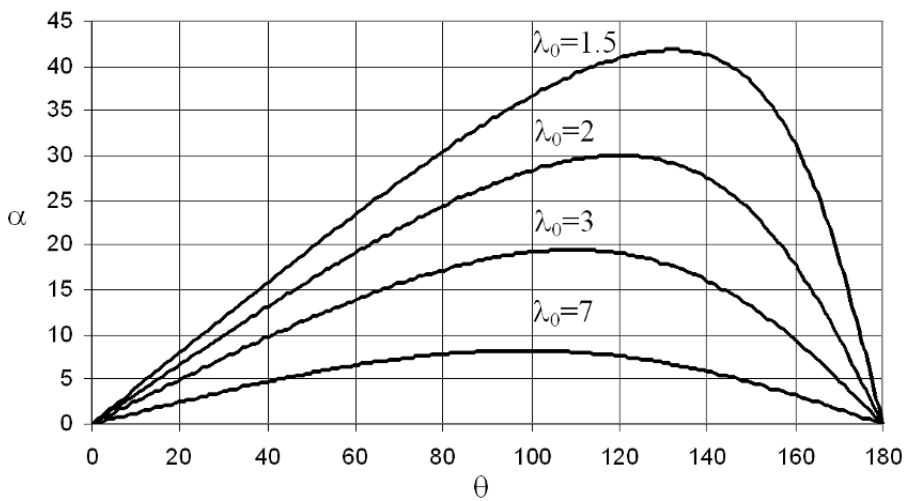

Figure 8.27. *Values of the angles of geometric incidence as a function of the angular position for different tip speed ratios λ_0*

Wind turbines function at optimal tip speed ratios of between 6 and 10. They are therefore only slightly affected by dynamic detachment. On the other hand, tidal turbines, which have wider blades, function at optimal tip speed ratios of between 2 and 4. They are therefore heavily affected by dynamic detachment. For tidal turbines, the point of optimal function (maximum C_P) corresponds to a flow which is greatly detached on a large portion of the disc of rotation.

Note that this analysis allows us to see the extent of detachment, but does not indicate whether the dynamic effects are significant or slight. This is crucial because if the dynamic effects remain slight, it is possible to construct models stationary simplified for Darrieus geometries, having the same basis as Glauert's model developed for axial geometries, in particular, the use of tables of lift and drag of the profiles is justified. Otherwise, we must resort to numerically modeling the Navier-Stokes equations, which is a more difficult task. To judge the dynamic characteristic of the flow, we need to judge the speed at which the incidence α varies when the blade moves. To do this, Laneville and Vittecoq [LAN 86] defined a reduced frequency F^* stemming from a study of helicopter blades:

$$F^* = \frac{c}{2\omega\, r\alpha_{max}} \left(\frac{d\alpha}{dt} \right)_{max} \qquad [8.22]$$

According to [MAC 72], dynamic effects begin to make themselves felt when F^* is greater than 0.05. In this case, the curve of lift depending on the incidence of the profile presents a hysteresis loop.

By inserting $\theta = \omega t$ into [8.21], we get:

$$\begin{cases} F^* = \dfrac{c}{2r\alpha_{max}\left(\lambda_0 - 1\right)} \\ \alpha_{max} = \tan^{-1}\left(\dfrac{1}{\sqrt{\lambda_0^2 - 1}} \right) \end{cases} \qquad [8.23]$$

Figure 8.28 presents F^* as a function of the chord-over-radius (c/r) relationship for the values of λ_0 considered above. For tidal turbines, c/r typically varies between 0.17 and 0.5. For these values, the figure shows that at the optimal tip speed ratios between 2 and 4 for transverse-flow tidal turbines, F^* may be far greater than 0.05. For the tidal turbine used by LEGI for their Ethic prototype (Figure 8.12c), we get $c/r = 0.37$ and optimal $\lambda_0 = 2$. The point representing the turbine is shown by a circle on the figure. For these values, F^* is equal to 0.35, which means that the

turbine is, at its optimum, in an area of pronounced detachment ($\lambda = 2$) and highly non-stationary ($F^* = 0.35$). Similarly, the two-bladed Darrieus wind turbine, 17 m in diameter, developed at the Sandia laboratories [WOR 78] is marked on the figure. The $c/r = 0.071$ and its optimal tip speed ratio λ_0 is 6. This turbine is scarcely subject to dynamic detachment at its optimal tip speed ratio and beyond it. Dynamic detachment only appears at lower tip speed ratios, but even then, the non-stationary effects remain slight.

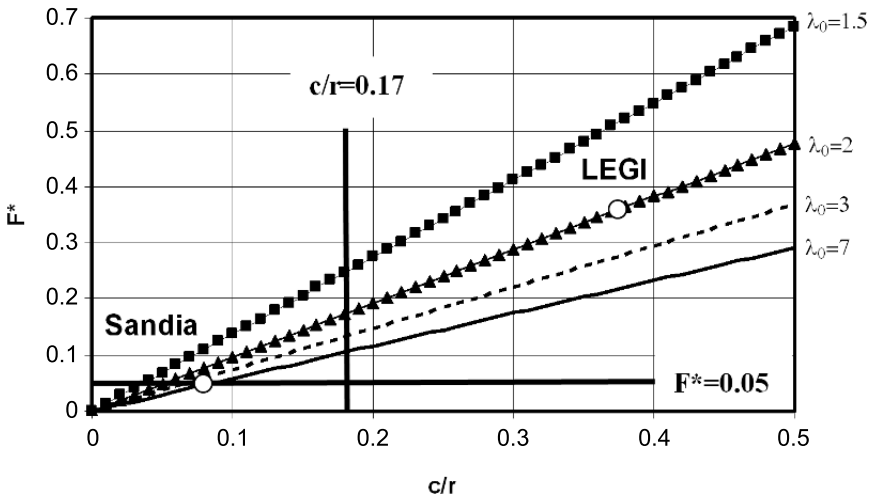

Figure 8.28. *Reduced frequency as a function of c/r and λ_0*

In conclusion, for the Sandia wind turbine, as for most Darrieus wind turbines, it is possible to use simplified stationary models through the introduction of corrections to allow dynamic detachment at low tip speed ratios to be taken into account. On the other hand, for transverse-flow tidal turbines, we must use a model in real fluid which solves the Navier-Stokes equations. However, the issue is obtaining sufficiently precise results at an acceptable calculation cost.

Figure 8.29 shows the vortex-type structures generated in the case of the two-bladed Darrieus wind turbine of Lanneville and Vittecoq [AME 09A]. A RANS (Reynold's Averaged Navier-Stokes Equation) numerical model associated with an SST k-ω turbulence model was used. The real elongation of the blades is 10 and c/r is 2. The turbine was designed with a tip speed ratio $\lambda_0 = 2$, which corresponds to a regime of intense dynamic detachment. The chord Reynold's number is 38,000. The vortex-type structures were identified using the Q criterion [HUN 88]. The Q criterion enables us to identify areas with high vorticity but low shearing rate of the

field of velocity; this allows us to eliminate the boundary layer regions in the interests of the vortexes carried in the flow.

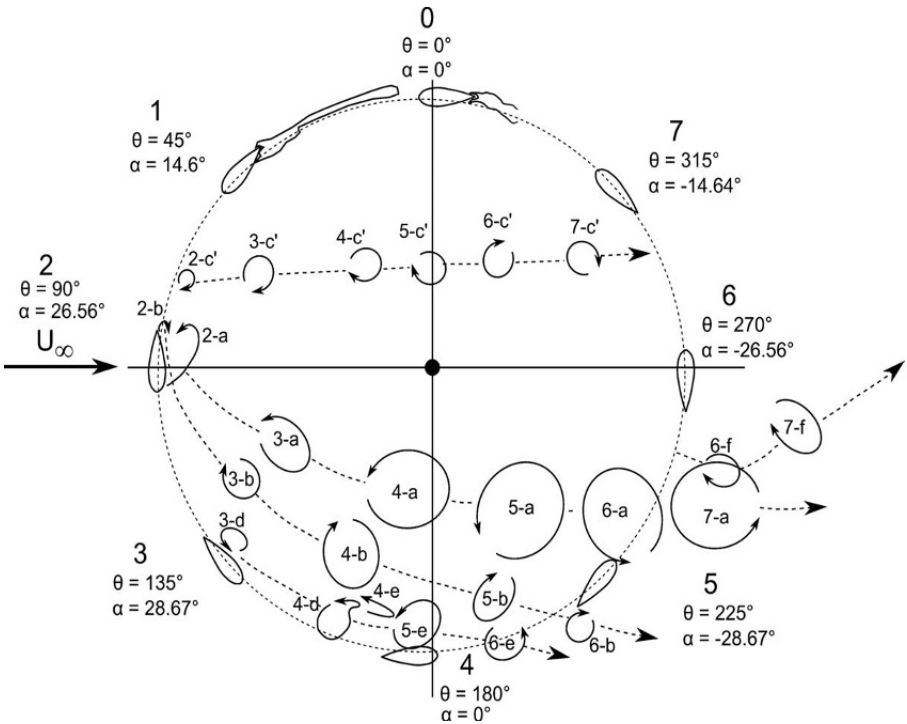

Figure 8.29. *Vortex-type structures obtained using the Q criterion [AME 09a]*

The calculated vorticity field is very rich. We find the vortex structures described by Brochier, especially the *a*-*b* counter-rotative vortex. The cycles of lift and drag obtained by the calculation are close to those experienced in real life. The LEGI tidal turbine was calculated by the same model in 2D and 3D configuration (Figure 8.30 left). As its diameter is equal to its height (17.5cm), the 3D effects are much stronger than in the case of Lannevilles' wind turbine. In 2D configuration, the average power coefficient obtained at the optimum is about 0.45, for an experimental value of about 0.35. Simulation in 3D configuration, which is more difficult to implement, yielded a power coefficient equal to 0.35. However, we should not imagine that the simulation is perfect; there is uncertainty about both the numerical model and the measurement of the performance of the tidal turbine. Regarding the calculation, the mesh, while it uses millions of cells, needs to be refined. In addition, weaknesses exist in the turbulence model: it does not represent

the laminar regions of the boundary layer on the profile and introduces a *numerical viscosity* which tends to dissipate vortex structures too quickly.

Figure 8.30 (right) illustrates the surfaces of iso-vorticity following the axis of rotation. The flow is from right to left and the turbine turns anticlockwise. We can clearly see the development of the *a* vortex on the internal face of the right-hand blades. We can also see the trace of these vortexes on the symmetrical plane as they move away from the blade which ejected them. The wing-tip vortex is also particularly visible. Finally, we can distinguish alternative Karman vortexes downstream of the axis of rotation.

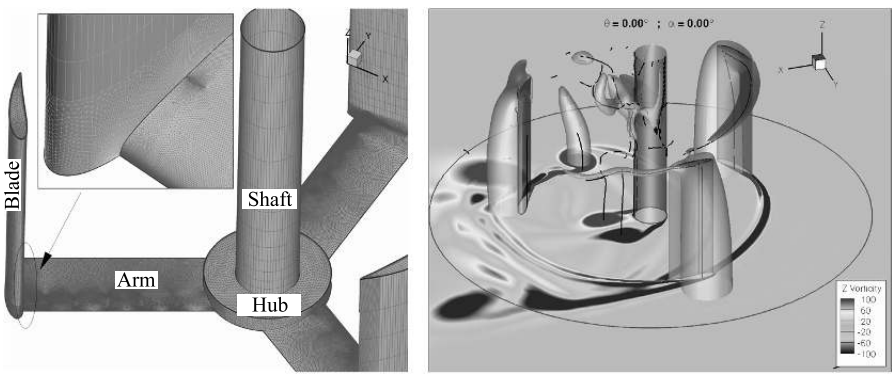

Figure 8.30. *LEGI tidal turbine (left); 3D model (right) [AME 09b]*

8.3.1.5. *Modeling the electrical generator*

There are a great many similarities between wind and tidal stream energy. That is why this book focuses mainly on the two reference electromechanical technologies used in the area of wind power. Both use doubly-fed induction generators and permanent magnet synchronous generators [BEN 09b], both operate at variable speed, enabling them to better exploit the turbine's performance and allowing it to function at the maximum C_p over a wide range of marine current speeds.

So as to control the velocity, a permanent magnet synchronous generator (PMSG) uses an alternating/continuous/alternating converter most often made of two IGBT bridges controlled by PWM, one of which is connected to the electrical grid and the other to the coils of the machine (Figure 8.31). The ability to make machines with a large number of poles allows for direct drive and does away with the gearbox needed in the following machines.

A doubly-fed induction generator (DFIG) may also be used to equip hydroelectric systems. In this case, the stator coils are directly connected to the grid while the speed of the generator is controlled by an alternating/ continuous/alternating converter which is connected to both the electrical grid and the rotor coils of the machine (Figure 8.32). The use of such a system based on a DFIG is common in the area of wind energy.

In fact, the converters used between the rotor and the grid are designed for around 30% of the generator's nominal power, which entails a not-insignificant reduction in the unwieldiness and total cost of the installation. On the other hand, the generator's excursion in terms of speed is limited within a range of ±50% around the machine's synchronous speed [BEN 09a]. This is not so with the PMSG, which allows for a wider range of variation in velocity at maximum torque until its nominal speed. This means that a PMSG can extract more energy than a DFIG by adapting the speed of the generator to that of the marine current, as per the strategy of maximum power point tracking (MPPT), across a wider range. The gain in energy extracted with PMSG as opposed to a DFIG, which is linked to the difference in excursion of speed, is then around 15-25% over a year depending on the nature of the installation site [BEN 10b].

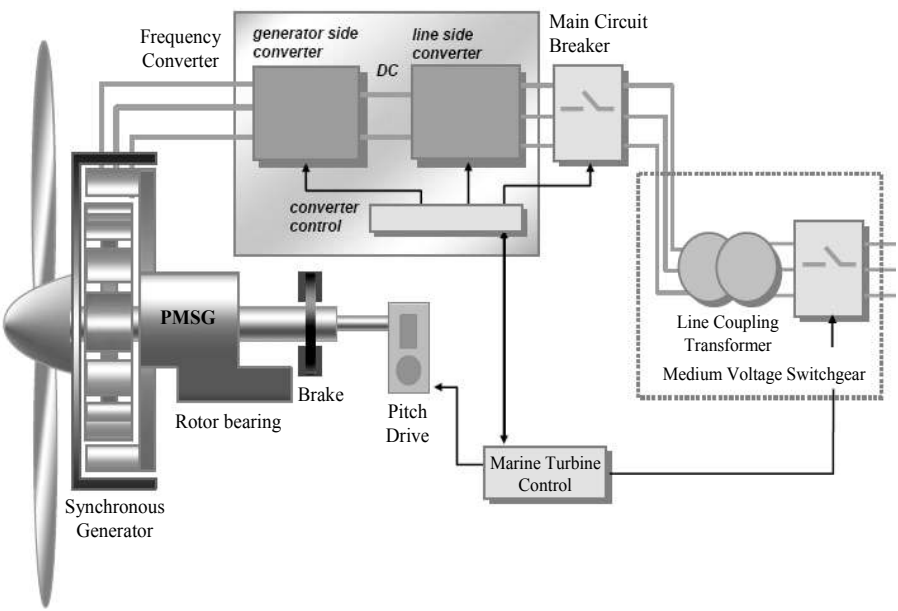

Figure 8.31. *Tidal turbine using a PMSG*

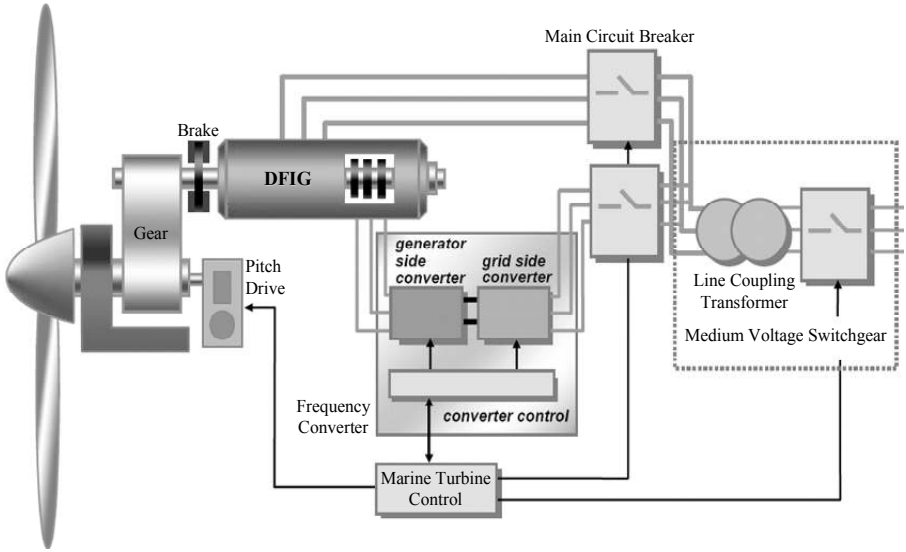

Figure 8.32. *Tidal turbine using a DFIG*

Apart from the difference in power generation that is related to a higher speed excursion for the PMSG, it should be noted that the DFIG seems slightly more advantageous than the PMSG in terms of acquisition cost because the ensemble of machine and converter is *a priori* less for a DFIG, which explains the success of these systems for wind power applications. However, the specific context of use at sea imposes different constraints. The tidal turbines will be submerged in places that are home to strong currents and are difficult to access. Minimizing maintenance aspects is therefore a fundamental concern. A direct-drive PMSG requires much less maintenance than a DFIG which includes a gearbox which must be drained at regular intervals and a system of blades and collars to feed the rotor. In addition, these systems have been observed to have higher failure rates in the field of wind energy [AMI 09]. It should be noted that, in order to further simplify the electromechanical transmission, it is also possible to directly integrate a permanent magnet synchronous generator in a nozzle surrounding the turbine. The propeller of the turbine then has a magnetic bolt with permanent magnets and is in this case the rotor of the generator. This solution provides a system which is *a priori* more compact and more robust than a conventional drive chain [DRO 10].

Figure 8.33 shows a diagram of this type of Rim Driven design. This design was adopted by the company OpenHydro chosen by EDF to supply the turbines for the experimental site Paimpol-Bréhat and the company Clean Current associated with Alstom Hydro.

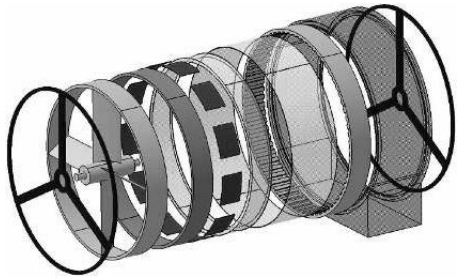

Figure 8.33. *Principle of a rim-driven integral generator*

Table 8.1 presents an overview of the comparative aspects of these two systems in the context of tidal turbines.

PMSG	DFIG
Advantages – Increased yields – No blades – Possibility of direct drive with no gearbox – Variable speed function across the whole range of power – Increased power per mass but with a gearbox – Minimized maintenance	*Advantages* – Power electronics designed at a fraction of the nominal power – Reduced combined cost of the converter and generator
Disadvantages – Power electronics designed for the nominal power of the generator – Large diameter of direct drive generator – Power electronics costly – High prices of permanent magnets	*Disadvantages* – Sliding brush-ring contacts – Limited range of speeds – Gearbox and brush-ring system requiring regular maintenance

Table 8.1. *Comparative aspects of PMSGs versus DFIGs*

The aim of the following paragraphs is to offer a synthetic presentation of the models (in a magnetically linear pattern) which can be used to design, control and simulate the converter-machine combinations associated with these two types of generators.

8.3.1.5.1. Doubly-fed induction generator

Modeling of a DFIG in view of its control is generally carried out in a rotating *d-q* reference frame using the following Park transformation, valid at the stator and the rotor.

$$\begin{bmatrix} V_d \\ V_q \end{bmatrix} = \frac{2}{3}\begin{bmatrix} \cos(-\theta_{s,r}) & \cos(-\theta_{s,r}+\frac{2\pi}{3}) & \cos(-\theta_{s,r}-\frac{2\pi}{3}) \\ \sin(-\theta_{s,r}) & \sin(-\theta_{s,r}+\frac{2\pi}{3}) & \sin(-\theta_{s,r}-\frac{2\pi}{3}) \end{bmatrix}\begin{bmatrix} V_a \\ V_b \\ V_v \end{bmatrix} \quad [8.24]$$

This transformation allows us to express the loads and flows according to equations [8.25] and [8.26], respectively. Note that hereafter, for ease of writing, these equations will be given in motor convention.

$$\begin{cases} V_{sd} = R_s i_{sd} + \frac{d}{dt}\phi_{sd} - \omega_s \phi_{sq} \\ V_{sq} = R_s i_{sq} + \frac{d}{dt}\phi_{sq} + \omega_s \phi_{sd} \\ V_{rd} = R_s i_{rd} + \frac{d}{dt}\phi_{rd} - (\omega_s - \omega)\phi_{rq} \\ V_{rq} = R_s i_{rq} + \frac{d}{dt}\phi_{rq} + (\omega_s - \omega)\phi_{rd} \end{cases} \quad [8.25]$$

$$\begin{cases} \phi_{sd} = L_s i_{sd} + M i_{rd} \\ \phi_{sq} = L_s i_{sq} + M i_{rq} \\ \phi_{rd} = L_r i_{rd} + M i_{sd} \\ \phi_{rq} = L_r i_{rq} + M i_{sq} \end{cases} \quad [8.26]$$

where R is the resistance, L and M represent the self and mutual inductances respectively, ω_s is the electrical speed of synchronicity and ω is the electrical speed of the rotor ($\omega = p.\Omega$ where p is the number of pairs of poles).

The expression of the electromagnetic torque is then given by:

$$T_{em} = \frac{3}{2} pM(i_{sq} i_{rd} - i_{rq} i_{sd}) \quad [8.27]$$

where p is the number of pairs of poles of the DFIG.

Finally, the mechanical equation is given by:

$$J \frac{d\Omega}{dt} = T_{em} - T_m - f\Omega \quad [8.28]$$

where J is inertia, Ω is the rotation speed, T_m is the mechanical torque and f is the viscous friction coefficient.

The equation set [8.25] to [8.28] thus represents a model which describes the electromechanical behavior of the DFIG and which can be used for simulations or to establish a schema of control.

8.3.1.5.2. Permanent magnet synchronous generator

Modeling of a permanent magnet synchronous generator in view of its control can also be carried out in a rotating *d-q* reference frame using Park transformation [8.24]. For the loads and flows, we then get equations [8.29] and [8.30], respectively.

$$\begin{cases} V_d = Ri_d + L_d \frac{di_d}{dt} - L_q i_q \omega_s \\ V_q = Ri_q + L_q \frac{di_q}{dt} + (L_d i_d + \phi_m)\omega_s \end{cases} \quad [8.29]$$

$$\begin{cases} \phi_d = L_d i_d + \phi_m \\ \phi_q = L_q i_q \end{cases} \quad [8.30]$$

where ϕ_m is the inductive flow produced by the permanent magnets. It should be noted that for a smooth-rotor PMSG (e.g. in surface-mounted magnet machines), $L_d = L_q$.

The general expression of the electromagnetic torque is given by:

$$T_{em} = \frac{3}{2} p[\phi_m i_q + (L_d - L_q) i_d i_q] \qquad [8.31]$$

The equation set [8.29] to [8.31], to which we must add the mechanical equation [8.28], then represents a model which describes the electromechanical behavior of the PMSG and which can be used for simulations or to establish a schema of control.

8.3.2. *Controlling elements of a tidal turbine*

The generator of a tidal turbine can, of course, be controlled using conventional PI or PID techniques. However, for obvious reasons of robustness as well as the imprecision of the modeling techniques and disturbances from the electrical grid, we shall give some details about how to apply gliding modes, which are greater.

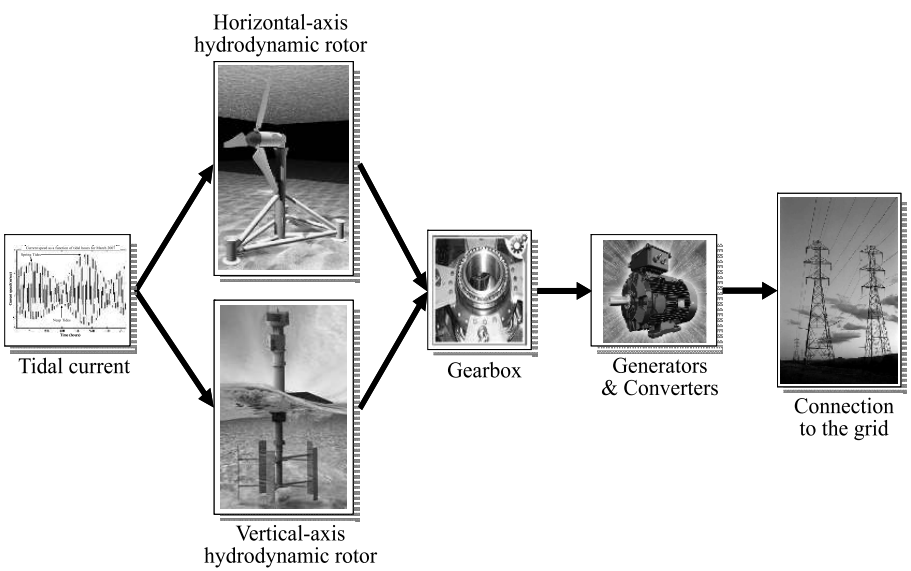

Figure 8.34. *Elements of integration of a tidal turbine*

The control techniques presented hereafter of course take account of the marine energy context, i.e. the resource and the horizontal-axis or vertical-axis collector (Figure 8.34). In addition, the effects of disturbances in the resource are taken into account by the Stockes model [8.4].

Like any generator system made up of parts arranged in a cascade, the control system can be broken down into four levels:

– so-called *close* control, which deals with the energetic components: inverters/rectifiers – generators – protection systems;

– so-called reference generating control, which involves generating the rules these different elements must obey: velocity, currents, voltage, frequencies;

– the layer of real-time adaptation to exogenous factors such as variations in tidal currents, disturbances in the grid, the algorithm maximum power point tracking;

– supervision, which defines the strategies pursued and which can be very simple (all available power injected into the electrical grid) or more complex, such as using it to power system services.

There are two modes of function:

– Injection of the power produced, to the full capability of the generator (maximum power point tracking – MPPT) or in a modulated manner so as to provide support to the grid, with or without controlling the reactive power;

– control of voltage (and frequency) with the aim of supplying power to isolated sites.

8.3.2.1. *Extraction of the maximum power*

The power characteristics compared to the speed of tidal currents and the speed of rotation of the turbine are similar to that of a wind turbine. Figures 8.35 and 8.36 illustrate this perfectly in the case of columns of Harvest-Ethic tidal turbines (Figure 8.12c) [AND 09a].

The difference lies more in the regularity of the current. The MPPT algorithms are therefore similar; between gradient type methods and *perturb and observe*, there is a wide range to choose from. The path to the maximum power point is simplified by the amortization of the viscous medium, within which the hydrodynamic collector evolves (Figure 8.37).

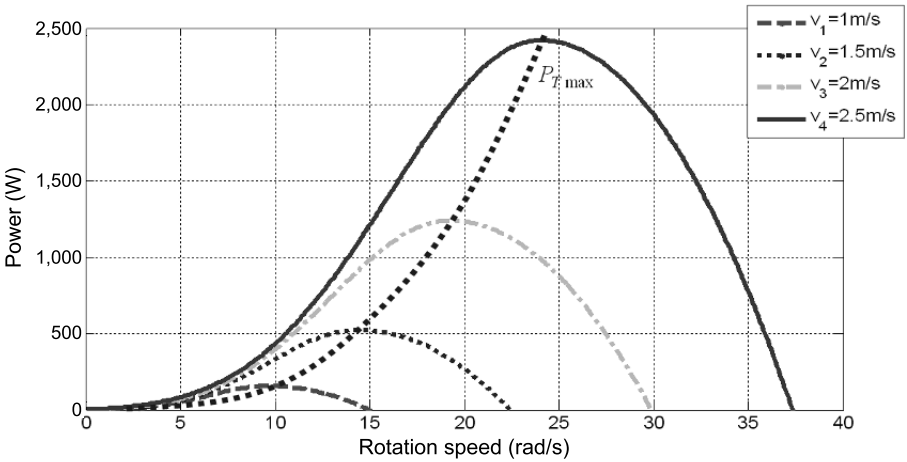

Figure 8.35. *Power characteristics of columns of Harvest-Ethic tidal turbines depending on the rotation speed for different water currents*

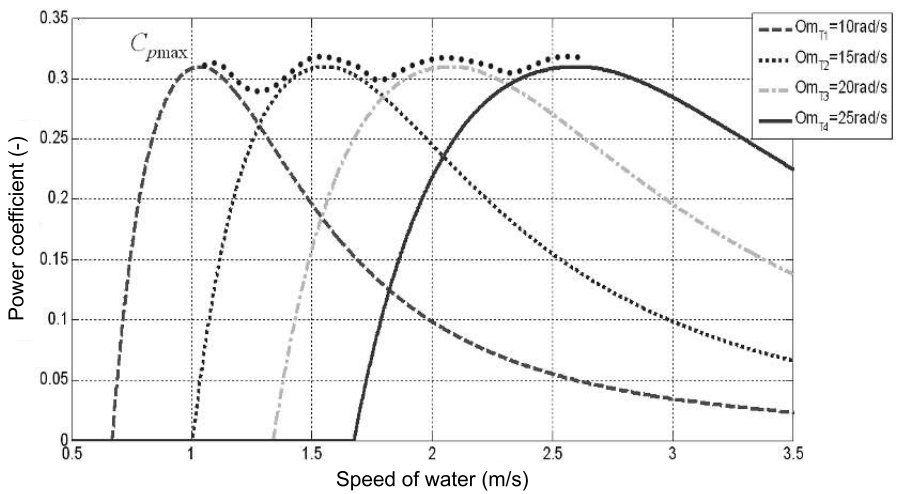

Figure 8.36. *Power coefficient depending on the water current for different rotation speeds*

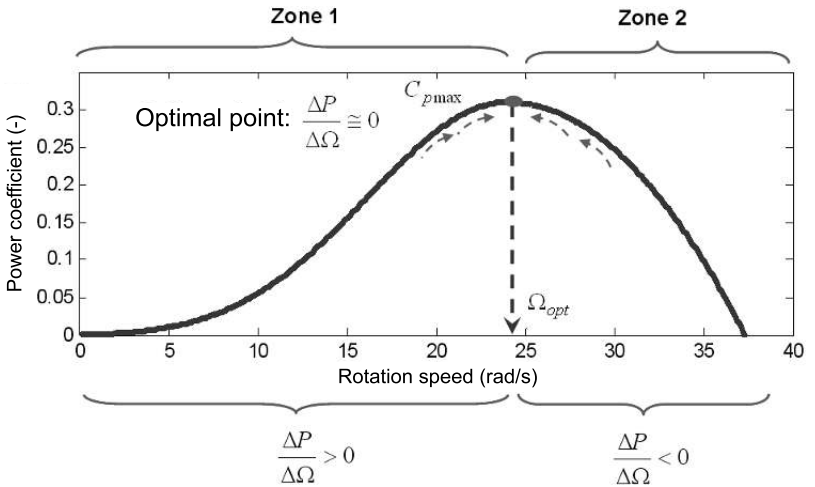

Figure 8.37. *Example of the path to the maximum power point based on the gradient [AND 09a]*

8.3.2.2. *Conventional controls*

In the following section, the orientation of the blades β is not taken into account, and we are looking only at tidal turbines with variable-speed generators.

8.3.2.2.1. Principles of optimal control of tidal turbines

In this case, optimization consists of using the characteristic curve $C_p(\lambda,\beta)$ (Figure 8.38). In general, the optimum $C_p(\lambda,\beta)$ is found using a look-up table.

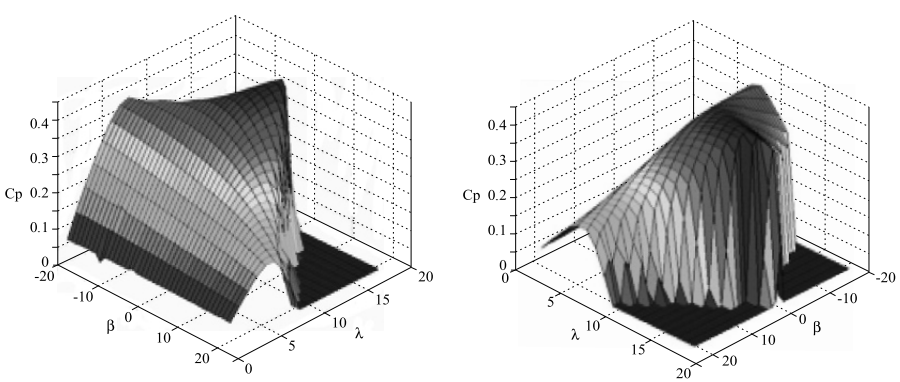

Figure 8.38. *Characteristic curves $C_p(\lambda,\beta)$ [BEN 09a]*

Fundamentally, control techniques vary depending on certain hypotheses having to do with the known parameters of the models, the measurable variables and the model of the tidal turbine. Depending on the richness of the modeling of the tidal turbine and in particular its torque characteristic, the following main approaches may be envisaged.

MPPT

This approach is appropriate when the parameters λ_{opt} and $C_{pmax} = C_p(\lambda_{opt})$ are unknown. In this case, the reference of velocity is adjusted so that the turbine functions at around its maximum power for a given speed of tidal current.

Optimal speed tracking using data from the turbine

This approach may be used if the optimal tip speed ratio λ_{opt} is known. This assumes the turbine has a speed regulating loop in order to attain the optimal speed:

$$\Omega_{ref} = \frac{\lambda_{opt}}{R} V(t) \qquad [8.32]$$

where R is the radius of the hydrodynamic collector.

Controlling the active power

This method is used when λ_{opt} and $C_{pmax} = C_p(\lambda_{opt})$ are known. The power extracted by the turbine can be written as follows:

$$P_{Turbine} = \frac{1}{2} C_p(\lambda) \rho \pi R^2 V^3 = \frac{1}{2} \frac{C_p(\lambda)}{\lambda^3} \rho \pi R^5 \Omega^3 \qquad [8.33]$$

By replacing λ_{opt} and $C_{pmax} = C_p(\lambda_{opt})$, we get the reference power:

$$\begin{cases} P_{Turbine_{opt}} = P_{ref} = K \Omega_{ref}^3 \\ K = \frac{1}{2} \frac{C_p(\lambda_{opt})}{\lambda_{opt}^3} \rho \pi R^5 \end{cases} \qquad [8.34]$$

This approach then assumes the use of a power regulating loop whose reference would be [8.34]. It is widely used in the field of wind energy and may be envisaged for tidal turbines.

8.3.2.2.2. Controlling the speed of a tidal turbine equipped with a DFIG

For simplicity's sake, we generally use a *d-q* reference frame linked to the rotating stator field and a stator flow aligned on the *d* axis ($\phi_{sq} = 0$). In addition, the stator resistance can be overlooked, given that this is a realistic hypothesis for the generators used in wind energy conversion. Using these considerations as a starting point, the expression of torque [8.27] becomes:

$$T_{em} = \frac{3}{2} p \frac{M}{L_s} \phi_{sd} I_{rq} \qquad [8.35]$$

In these conditions, Park's model of a DFIG is illustrated by Figure 8.39.

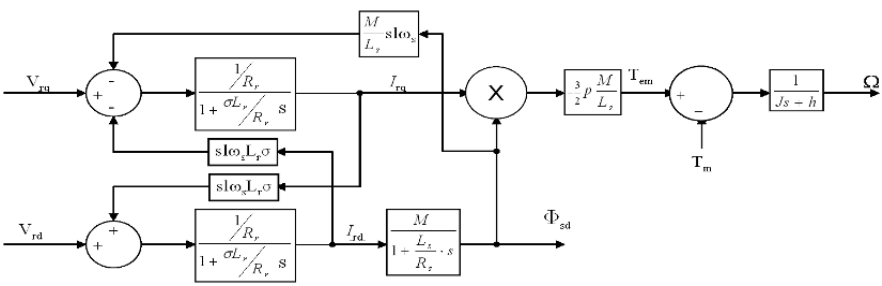

Figure 8.39. *Park's model of a DFIG*

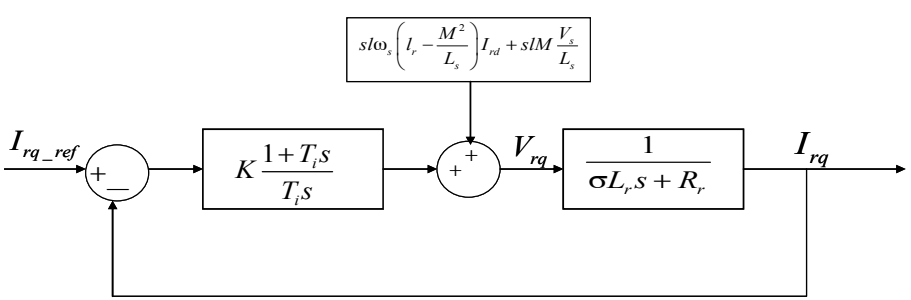

Figure 8.40. *Internal loop controlling the speed of a DFIG*

This figure shows that the control could be carried out by the rotoric current i_{rq}. An internal current loop is then needed (Figure 8.40). In addition, having dynamics on different scales (electrical and mechanical) it is wise to control the DFIG in a cascade, with the current loop inside. Speed control is then added, in an external loop (Figure 8.41).

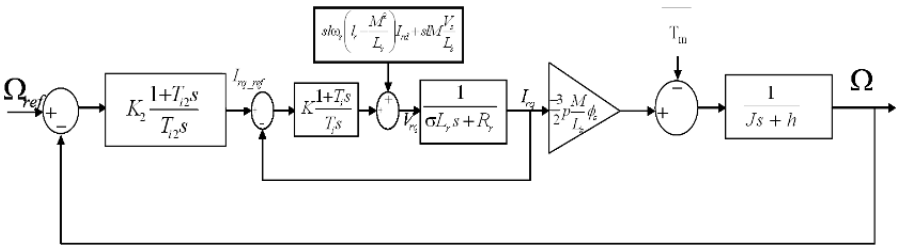

Figure 8.41. *Control of a DFIG in a cascade*

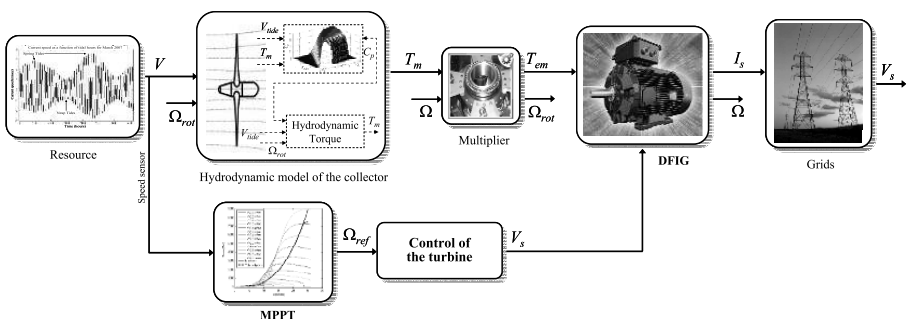

Figure 8.42. *Controlling the speed of a horizontal-axis tidal turbine so as to function at the maximum recoverable power*

The principle of controlling the speed of a horizontal-axis tidal turbine is illustrated by Figure 8.42. It was tested on an experimental tidal turbine, 1.44 m in diameter and with a 7.5 kW power capacity, with tidal current data collected from the Raz de Sein site [BEN 07]. Thus, for a profile of tidal current speed given by Figure 8.43 and therefore a speed reference taken using the MPPT strategy, Figures 8.44 and 8.45 illustrate control performances.

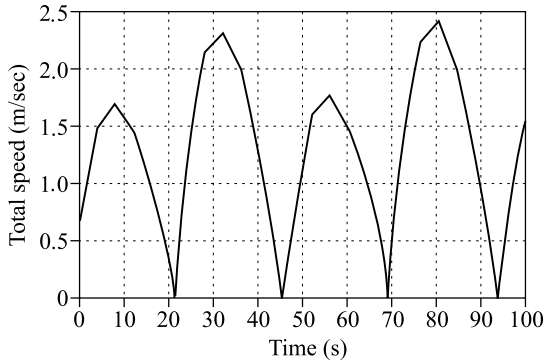

Figure 8.43. *Profile of tidal current speeds*

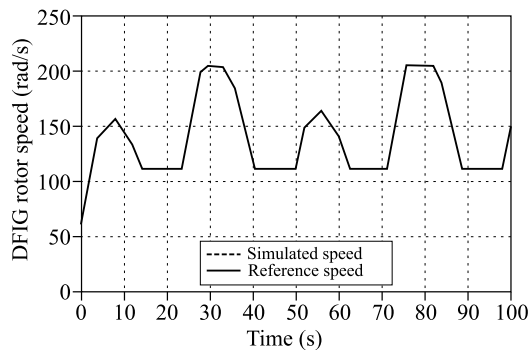

Figure 8.44. *Rotor speed of a DFIG*

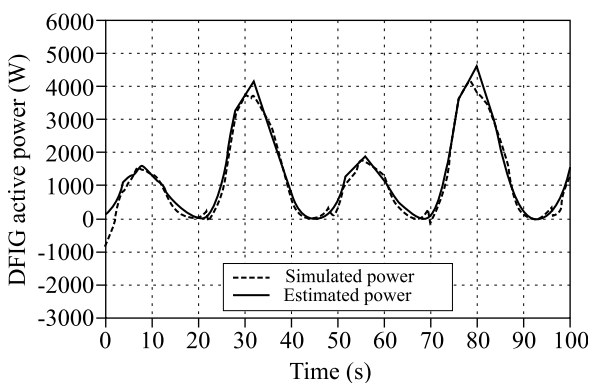

Figure 8.45. *Power generated by a DFIG*

8.3.2.2.3. Controlling the speed of a tidal turbine fitted with a PMSG

Conventionally, a *d-q* reference frame linked to the rotating stator field is used. Also, for a PMSG, where $L_d = L_q$. the torque expression [8.31] becomes:

$$T_{em} = \frac{3}{2} p \phi_m i_q \qquad [8.36]$$

In these conditions, Park's model of a PMSG is illustrated by Figure 8.46. The same control strategy may also be used for a tidal turbine with a PMSG. This necessitates an internal loop for the current i_{rq} and an external loop for the speed.

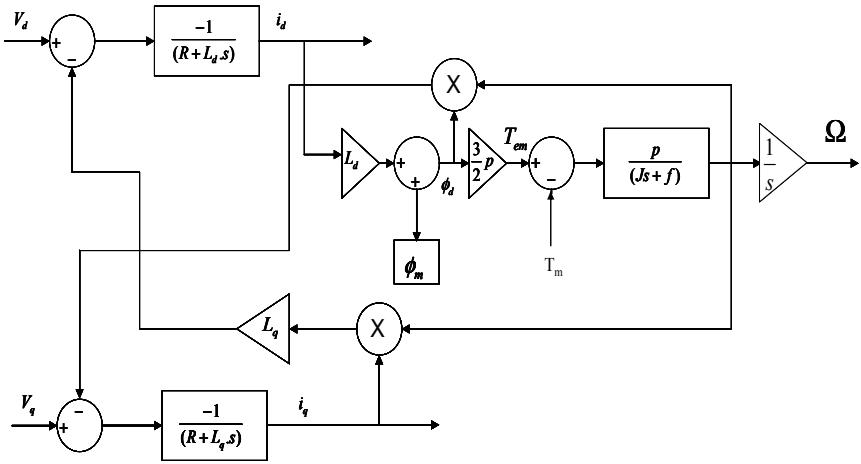

Figure 8.46. *Park's model of a PMSG*

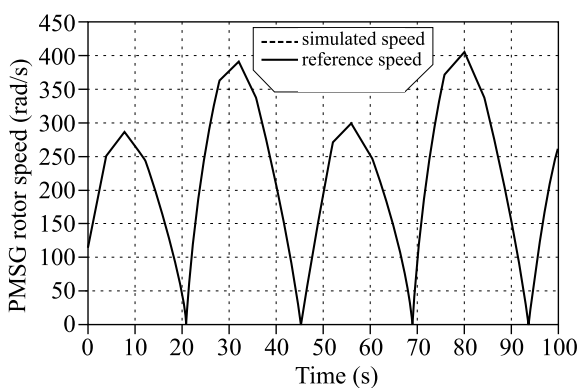

Figure 8.47. *Rotor speed of a PMSG*

With regard to the same horizontal-axis tidal turbine and the same current data as for the site at Raz de Sein, Figures 8.47 and 8.48 illustrate the performance of the control system, for a speed reference generated using MPPT (with the same tidal current speed profile as given in Figure 8.43).

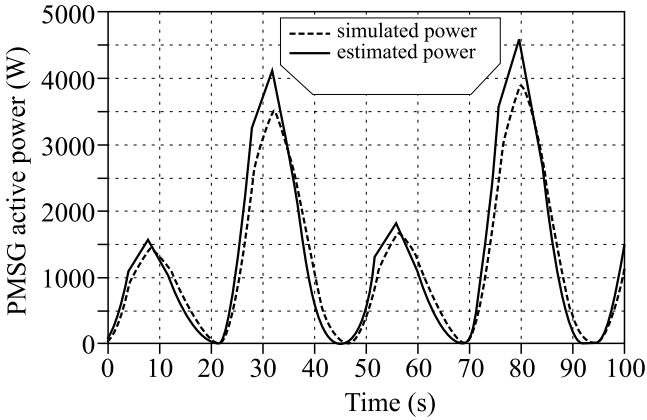

Figure 8.48. *Power generated by a PMSG*

8.3.2.2.4. Illustration of the control system for a vertical-axis tidal turbine

In the following section we illustrate other approaches to controlling a vertical-axis tidal turbine – in particular, control of the continuous bus voltage. In this case, it is controlled by the generator-side inverter for isolated network supply (*Vf* mode) and by the network-side inverter for injection of the electricity into a powerful grid (*PQ* mode) [AND 08], [AND 09a], [AND 09b].

Vf mode

The upstream energy chain adapts the rotation speed of the turbine Ω to modulate the power extracted, in order to maintain the continuous bus voltage U_{DC} at a sufficient value. However, it must be noted that with regulation, one must be careful to remain on the left-hand side of the turbine's bell curve (Figure 8.37).

PQ mode

In this case, the U_{DC} voltage is regulated by the continuous current entering the network-side inverter. The system may be configured in a number of ways. In Figure 8.49, the voltage corrector (H_{PI}) directly generates the reference from the active component of the current injected into the grid, i_{qres}. The inverter is assimilated to a gain G_{OND}, the continuous bus is represented by the filtering torque C_{DC}, R_{DC}, the currents I_{DCred} and I_{DCond} are respectively given by the generator-side

and network-side inverters, and finally L_f and R_f denote the filter of connection to the grid, whose voltage is here notated v_{res}.

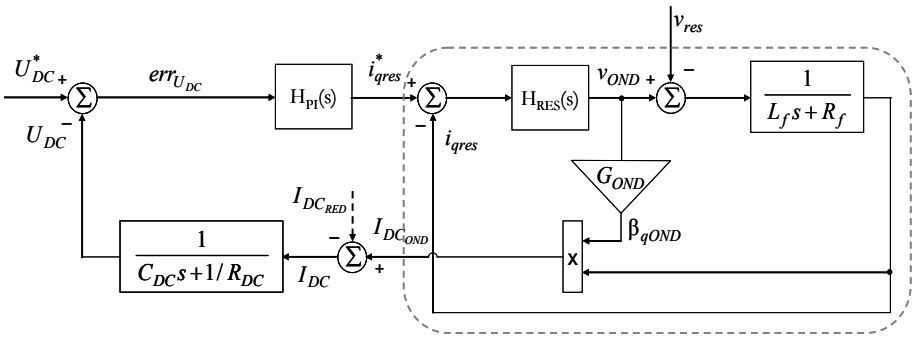

Figure 8.49. *Controlling the continuous bus voltage by injecting the active current into the grid*

Figures 8.50 and 8.51 give an overview of the two modes of operation discussed above. We can clearly distinguish the differences in terms of the control of the DC bus voltage and of the dissipater which is present in *PQ* mode and is activated if the energy produced cannot be transferred to the grid.

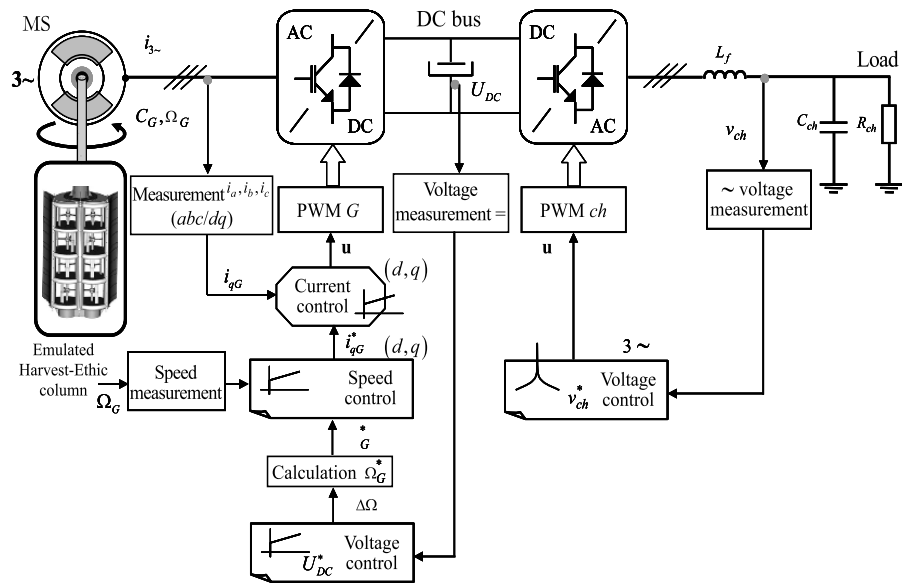

Figure 8.50. *Vf mode*

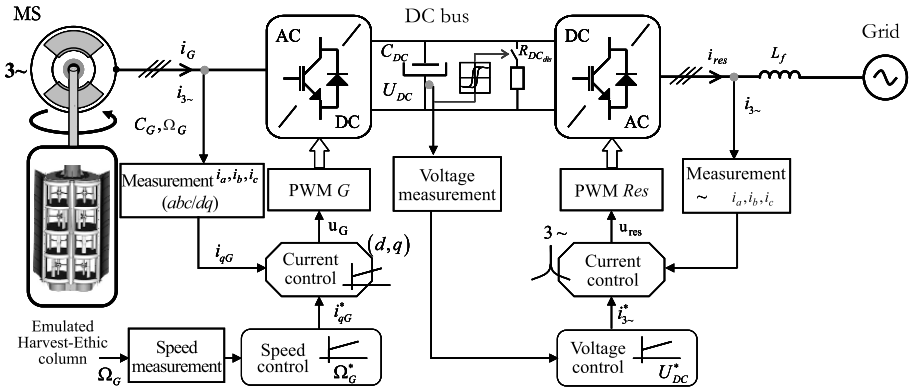

Figure 8.51. *PQ mode*

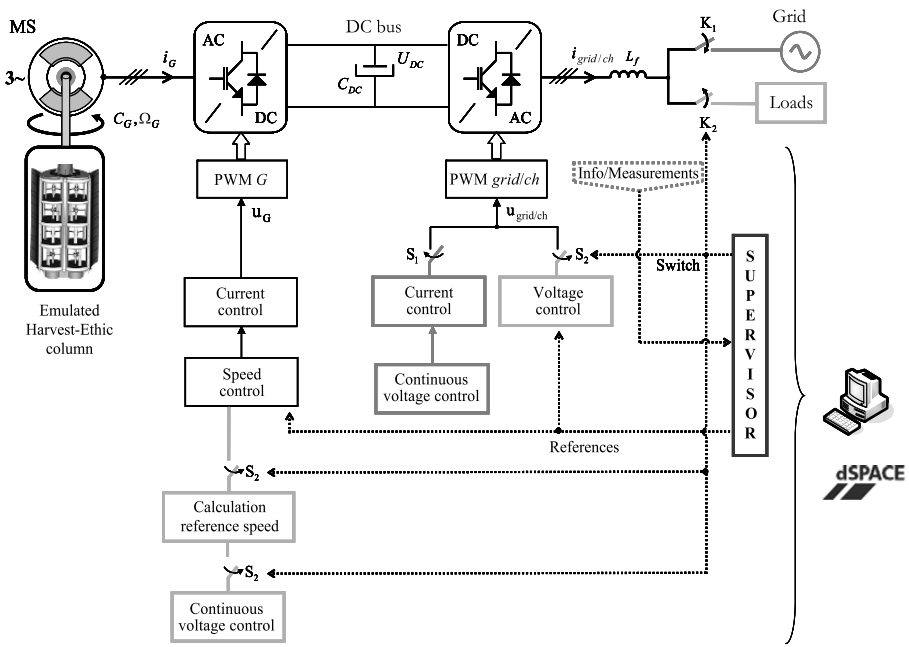

Figure 8.52. *Overview of the laws of control and piloting for the PQ-Vf-PQ transition*

It is also possible to switch between the two modes because, unlike for a wind turbine, the regularity of tidal currents allows the machine to function in island

mode and also acts as a safety supply in case of grid failure, along with energy storage elements. The transitions are easily carried out. However, one must choose the moment for the switch when the grid is back online well, so as to control the transients (Figure 8.52).

8.3.2.3. *Advanced controlling elements*

Above, so-called conventional PI controls were used to monitor the velocity of a tidal turbine equipped with either a DFIG or a PMSG. This type of regulator is well-known for its simplicity with constant references. However, in the case of marine turbines, the reference signals generated vary over time, and tidal currents may be turbulent. This would obviously have an adverse effect on the performance of PI control.

In addition, in any formulation of a control problem, the mathematical model developed in order to establish the law of control does not reflect the real-world process exactly. These differences may, for example, be due to dynamics which have not been modeled, variations in the system's parameters or too general a way of modeling the complex behaviors of the process. Nevertheless, in spite of all these inaccuracies, the resulting law of control must be capable of meeting the predefined goals. This has led to there being a particular advantage to creating so-called robust controls which are capable of overcoming this problem.

Indeed, the limits of the approach using PID-type linear correctors soon became evident. These linear correctors are subject to Bode's law, which dictates that the amplitude effects and phase effects are coupled and antagonistic. For example, any advance in phase, which is the beneficial effect being sought, is necessarily accompanied by an increase in the dynamic relation. In fact, the possibilities of compensating and using increased gains are thereby reduced.

In order to overcome these disadvantages, we can envisage nonlinear techniques, such as adaption of absolute stability methods, but also sliding mode control. This latter is to be found in the theory of variable structure systems. The laws of control by sliding modes are written so as to keep the system close to a sliding surface.

There are two main advantages to such an approach. Firstly, the dynamic behavior which results may be determined by choosing an appropriate surface. Secondly, the system's response in a closed loop is completely impervious to a particular type of uncertainty, making this method a serious contender in the search for ways to create robust controls for hydroelectric systems. In this context, work carried out on horizontal-axis tidal turbines with a DFIG or a PMSG clearly shows the advantages and improvements obtained using higher-order (2^{nd} order) sliding modes in comparison with PI regulators [FRI 02], [BEN 10b], [BEN 11].

In order to create a variable-speed control system based on MPPT, we must generate a reference electromagnetic torque $T_{em\text{-}ref}$ using the rotation speed Ω_{ref} (Figure 8.53).

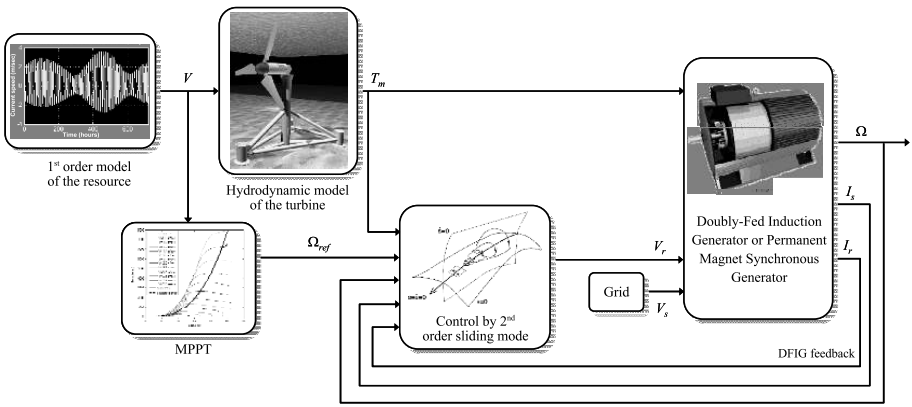

Figure 8.53. *Overview of speed control of a tidal turbine with a DFIG or a PMSG by higher-order sliding modes*

$$T_{em\_ref} = T_m + h\Omega - \alpha(\Omega - \omega_{ref}) + J\dot{\Omega}_{ref} \qquad [8.37]$$

In addition, the sliding surfaces S_1 and S_2 are defined so as to ensure control of the rotation speed and the reactive power. Control of a DFIG is described by the following equations:

$$\begin{cases} I_{qr\_ref} = -\dfrac{L_s}{pM}\dfrac{T_{em\_ref}}{\phi_{sd}} \\ I_{dr\_ref} = \dfrac{1}{M}\phi_{sd} \end{cases} \qquad [8.38]$$

$$\begin{cases} S_1 = I_{dr} - I_{dr\_ref} \\ S_2 = I_{qr} - I_{qr\_ref} \end{cases} \qquad [8.39]$$

$$\begin{cases} \dot{S}_1 = \dfrac{L_s}{M^2 - L_r L_s}\left(V_{dr} + R_r I_{dr} - \omega_r (L_r I_{qr} + M I_{qs}) - \dfrac{M}{L_s} V_{ds} \right. \\ \qquad \left. - \dfrac{M R_s}{L_s} I_{ds} + \dfrac{M}{L_s} \omega_s \left(L_s I_{qs} + M I_{qr} \right) \right) - \dot{I}_{dr\_ref} \\ \ddot{S}_1 = \varphi_1(t,x) + \gamma_1(t,x) \dot{V}_{dr} \\ \dot{S}_2 = \dfrac{L_s}{M^2 - L_r L_s}\left(V_{qr} + R_r I_{qr} + \omega_r (L_r I_{dr} + M I_{ds}) - \dfrac{M}{L_s} V_{qs} \right. \\ \qquad \left. - \dfrac{M R_s}{L_s} I_{qs} - \dfrac{M}{L_s} \omega_s \left(L_s I_{ds} + M I_{dr} \right) \right) - \dot{I}_{qr\_ref} \\ \ddot{S}_2 = \varphi_2(t,x) + \gamma_2(t,x) \dot{V}_{qr} \end{cases} \quad [8.40]$$

Equations [8.41] to [8.43] in turn describe the control of a PMSG.

$$\begin{cases} I_{d\_ref} = 0 \\ I_{q\_ref} = \dfrac{2}{3} \dfrac{T_{em}}{p \phi_f} \end{cases} \quad [8.41]$$

$$\begin{cases} S_1 = I_d - I_{d\_ref} \\ S_2 = I_q - I_{q\_ref} \end{cases} \quad [8.42]$$

$$\begin{cases} \dot{S}_1 = \dot{I}_d - \dot{I}_{d\_ref} \\ \ddot{S}_1 = \varphi_1(t,x) + \gamma_1(t,x) \dot{V}_d \\ \dot{S}_2 = \dot{I}_q - \dot{I}_{q\_ref} \\ \ddot{S}_2 = \varphi_2(t,x) + \gamma_2(t,x) \dot{V}_q \end{cases} \quad [8.43]$$

These two controls were tested on the same experimental tidal turbine, 1.44 m in diameter and with 7.5 kW of power, with tidal current data gleaned from the site at Raz de Sein [BEN 07]. Thus, for a speed reference generated using MPPT, Figures 8.54 and 8.55 illustrate performances in the case of a DFIG (with the same tidal current speed profile as given in Figure 8.43).

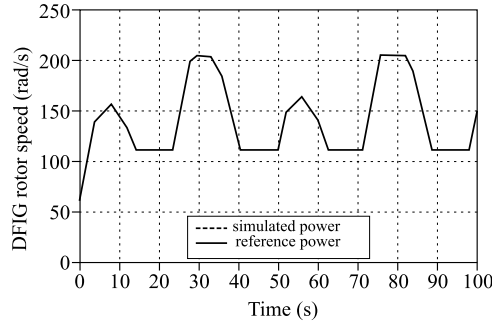

Figure 8.54. *Rotor speed of a DFIG*

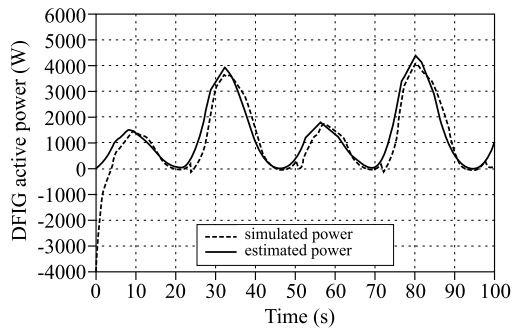

Figure 8.55. *Power generated by a DFIG*

Figures 8.56 and 8.57 in turn illustrate the performance of the control system in the case of a PMSG.

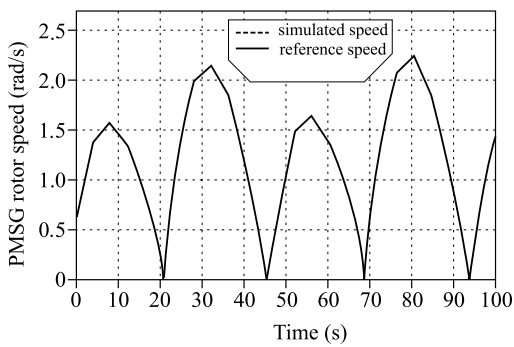

Figure 8.56. *Rotor speed of a PMSG*

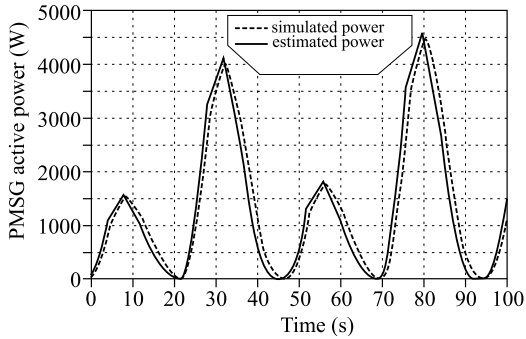

Figure 8.57. *Power generated by a PMSG*

8.4. Bibliography

[ABB 59] ABBOT H., VON DOENHOFF, A.E., *Theory of Wing Sections*, Dover Publications, New York, 1959

[AME 09a] AMET E., MAITRE T., PELLONE, C., ACHARD J.L., "2D numerical simulations of blade-vortex interaction in a Darrieus turbine", *Journal of Fluids Engineering*, vol. 131, 111103-1, November 2009.

[AME 09b] AMET E., Simulation numérique d'une tidal turbine à axe vertical de type Darrieus, PhD Thesis, Polytechnic Institute of Grenoble and the Bucharest University of Construction Technique, May 2009.

[AMI 09] AMIRAT Y., BENBOUZID M.E.H., AL-AHMAR E., BENSAKER B., TURRI S., "A brief status on condition monitoring and fault diagnosis in wind energy conversion systems", *Elsevier Renewable & Sustainable Energy Reviews*, vol. 3, no. 9, pp. 2629-2636, December 2009.

[AND 08] ANDREICA M., BACHA S., ROYE D., Exteberria-Otadui I., "Micro-hydro water Current turbine control for grid connected or islanding operation", *Proceedings of the 2008 IEEE PESC*, pp. 952-962, Rhodes, Greece, June 2008.

[AND 09a] ANDREICA M., Optimisation énergétique de chaînes de conversion tidal turbines, modélisation, commandes et réalisations expérimentales, PhD Thesis, Polytechnic Institute of Grenoble, July 2009.

[AND 09b] ANDREICA M., BACHA S., ROYE D., MUNTEANU I., BRATCU A.I., GUIRAUD J., "Stand-alone operation of cross-flow water turbines", *Proceedings of the 2009 IEEE ICIT*, pp. 1-6, Churchill, Australia, February 2009.

[BEN 07] BENELGHALI S., BALME R., LE SAUX K., BENBOUZID M.E.H., CHARPENTIER J.F., HAUVILLE F., "A simulation model for the evaluation of the electrical power potential harnessed by a marine current turbine", *IEEE Journal on Oceanic Engineering*, vol. 32, no. 4, pp. 786-797, October 2007.

[BEN 08] BENELGHALI S., DROUEN L., BENBOUZID M.E.H., CHARPENTIER J.F., ASTOLFI J.A., HAUVILLE F., "Les systèmes de génération d'énergie électrique à partir des courants de marées", *Revue 3EI*, no. 52, pp. 73-85, March 2008.

[BEN 09a] BENELGHALI S., On multiphysics modeling and control of marine current turbine systems, PhD Thesis, University of Brest, December 2009.

[BEN 09b] BENELGHALI S., BENBOUZID M.E.H., CHARPENTIER J.F., "Marine tidal current electric power generation technology – a review", *Electromotion*, vol. 16, no. 3, pp. 155-166, July-September 2009.

[BEN 10a] BENELGHALI S., BENBOUZID M.E.H., CHARPENTIER J.F., "Modeling and control of a marine current turbine driven doubly-fed induction generator", *IET Renewable Power Generation*, vol. 4, no. 1, pp. 1-11, January 2010.

[BEN 10b] BENELGHALI S., BENBOUZID M.E.H., CHARPENTIER J.F., "Comparison of PMSG and DFIG for marine current turbine applications", *Proceedings of ICEM'10*, pp. 1-6, Rome, Italy, September 2010.

[BEN 10c] BENELGHALI S., BENBOUZID M.E.H., AHMED-ALI T., CHARPENTIER J.F., "High-order sliding mode control of a marine current turbine driven doubly-fed induction generator", *IEEE Journal of Oceanic Engineering*, vol. 35, no. 2, pp. 402-411, April 2010.

[BEN 11] BENELGHALI S., BENBOUZID M.E.H., CHARPENTIER J.F., AHMED-ALI T., MUNTEANU I., "Experimental validation of a marine current turbine simulator: application to a PMSG-based system second-order sliding mode control", *IEEE Transactions on Industrial Electronics*, vol. 58, no. 1, pp. 118-126, January 2011.

[BER 08] BERNITSAS M.M., RAGHAVAN K., BEN-SIMON Y., GARCIA E.M.H., "VIVACE (Vortex Induced Vibration Aquatic Clean Energy): A new concept in generation of clean and renewable energy from fluid flow", *Journal of Offshore Mechanics and Arctic Engineering*, vol. 130, no. 4, 2008.

[BRO 86] BROCHIER, G., FRAUNIÉ, P., BÉGUIER, C., PARASCHIVOIU, I., "Water channel experiments of dynamic stall on darrieus wind turbine blades", *Journal of Propulsion*, vol. 2, no. 5, pp. 445-449, September-October 1986.

[BRY 04] BRYDEN I.G. *et al.*, "Choosing and evaluating sites for tidal current development", *Proc. IMechE*, *Part A: Journal of Power and Energy*, vol. 218, no. 8, pp. 567-578, 2004.

[DRO 10] DROUEN L., Machines électriques intégrées à des hélices marines: Contribution à une modélisation et conception multi-physique, PhD Thesis, ENSAM ParisTech, December 2010.

[EU 96] EU COMMISSION, The exploitation of tidal marine currents, Report EUR16683EN, 1996.

[FRI 02] FRIDMAN L., LEVANT A., "Higher order sliding modes", Chapter 3 in *Sliding Mode Control in Engineering*, Marcel Dekker, Inc., pp. 53-101, 2002.

[GLA 35] GLAUERT, H., *Airplane propellers*, in DURAND W.F. (ed.), *Aerodynamic Theory*, vol. 4, Division L, Julius Springer, Berlin, pp. 169-360, 1935.

[HAM 93] HAMMONS T.J., "Tidal power", *Proc. IEEE*, vol. 3, no. 8, pp. 419-433, March 1993.

[HUN 88] HUNT, J.C.R., WRAY A.A., MOIN, P., "Eddies, streams, and convergence zones in turbulent flows", *CTR-S88*, pp. 193-208, 1988.

[JOH 06] JOHNSTONE C.M. *et al.*, "EC FPVI co-ordinated action on ocean energy: a European platform for sharing technical information and research outcomes in wave and tidal energy systems," *Renewable Energy*, vol. 31, pp. 191-196, 2006.

[KHA 09] KHAN M.J., BHUYAN G., IQBAL M.T., QUAICOE J.E., "Hydrokinetic energy conversion systems and assessment of horizontal and vertical axis turbines for river and tidal applications: A technology status review", *Applied Energy*, vol. 86, no. 10, pp. 1823-1835, October 2009.

[KIR 05] KIRKE B., Developments in ducted water current turbines, http://www.cyberiad.net/library/pdf/bk_tidal_paper25apr06.pdf, 2005.

[LAN 86] LANEVILLE A., VITTECOQ P., "Dynamic stall: The case of the vertical axis wind turbine", *Journal of Solar Energy Engineering*, vol. 108, pp. 140-145, 1986.

[LEG 08] LE GOURIERES D., *Les éoliennes: Théorie, Conception et Calcul Pratique*, Moulin Cadiou, France, 2008.

[MAC 72] MC CROSKEY W.J., "Dynamic stall on airfoils and helicopters rotors", *AGARD Paper*, no. R595, 1972.

[PAR 02] PARASCHIVOIU I., *Wind Turbine Design with Emphasis on the Darrieus Concept*, Polytechnic International Press, Montreal, Canada, 2002.

[SAH 06] SAHA U.K., JAYA RAJKUMAR M., "On the performance analysis of Savonius rotor with twisted blades", *Renewable Energy*, vol. 31, no. 11, pp. 1776-1788, September 2006.

[WOR 78] WORSTELL M.H., Aerodynamic Performance of the 17-m Diameter Darrieus Wind Turbine, Sandia Report AND78-1737 l, September 1978.